Jiang, Shuai-Qing, Xu, Dong, van Hoof, Agnes P. C., Lei, Wei-Hua, Liu, Yuan, Zhou, Hao, Chen, Yong, Fu, Shao-Yu, Yang, Jun, Liu, Xing, Zhu, Zi-Pei, Filippenko, Alexei V., Jonker, Peter G., Pozanenko, A. S., Gao, He, Wu, Xue-Feng, Zhang, Bing, Lamb, Gavin P, De Pasquale, Massimiliano, Kobayashi, Shiho, Bauer, Franz Erik, Sun, Hui, Pugliese, Giovanna, An, Jie, D'Elia, Valerio, Fynbo, Johan P. U., Zheng, WeiKang, Castro-Tirado, Alberto J., Yin, Yi-Han Iris, Zou, Yuan-Chuan, Deller, Adam T., Pankov, N. S., Volnova, A. A., Moskvitin, A. S., Spiridonova, O. I., Oparin, D. V., Rumyantsev, V., Burkhonov, O. A., Egamberdiyev, Sh. A., Kim, V., Krugov, M., Tatarnikov, A. M., Inasaridze, R., Levan, Andrew J., Malesani, Daniele Bjørn, Ravasio, Maria E., Quirola-Vásquez, Jonathan, van Dalen, Joyce N. D., Sánchez-Sierras, Javi, Mata Sánchez, Daniel, Littlefair, Stuart P., Chacón, Jennifer A., Torres, Manuel A. P., Chrimes, Ashley A., Sarin, Nikhil, Martin-Carrillo, Antonio, Dhillon, Vik, Yang, Yi, Brink, Thomas G., Davies, Rebecca L., Yang, Sheng, Aryan, Amar, Chen, Ting-Wan, Kong, Albert K. H., Li, Wen-Xiong, Li, Rui-Zhi, Mao, Jirong, Pérez-García, Ignacio, Fernández-García, Emilio J., Andrews, Moira, Farah, Joseph, Fan, Zhou, Padilla Gonzalez, Estefania, Howell, D. Andrew, Hartmann, Dieter, Hu, Jing-Wei, Jakobsson, Páll, Li, Cheng-Kui, Ling, Zhi-Xing, McCully, Curtis, Newsome, Megan, Schneider, Benjamin, Tinyanont, Kaew Samaporn, Sun, Ning-Chen, Terreran, Giacomo, Tang, Qing-Wen, Wang, Wen-Xin, Xu, Jing-Jing, Yuan, Wei-Min, Zhang, Bin-Bin, Zhao, Hai-Sheng and Zhang, Juan

EP240801a/XRF 240801B: An X-Ray Flash Detected by the Einstein Probe and the Implications of Its Multiband Afterglow

Article

The Astrophysical Journal Letters, 988:L34 (18pp), 2025 July 20 https://doi.org/10.3847/2041-8213/addebf

EP240801a/XRF 240801B: An X-Ray Flash Detected by the Einstein Probe and the Implications of Its Multiband Afterglow

Shuai-Qing Jiang[1,2], Dong Xu[1,3], Agnes P. C. van Hoof[4], Wei-Hua Lei[5], Yuan Liu[1], Hao Zhou[6], Yong Chen[7], Shao-Yu Fu[1], Jun Yang[8,9], Xing Liu[1,2], Zi-Pei Zhu[1], Alexei V. Filippenko[10], Peter G. Jonker[4], A. S. Pozanenko[11,12,13], He Gao[14,15], Xue-Feng Wu[6], Bing Zhang[16,17], Gavin P Lamb[18], Massimiliano De Pasquale[19], Shiho Kobayashi[18], Franz Erik Bauer[20], Hui Sun[1], Giovanna Pugliese[21], Jie An[1,2], Valerio D'Elia[22,23], Johan P. U. Fynbo[24,25], WeiKang Zheng[10], Alberto J. Castro-Tirado[26,27], Yi-Han Iris Yin[8,9], Yuan-Chuan Zou[5], Adam T. Deller[28,29], N. S. Pankov[11,12], A. A. Volnova[11], A. S. Moskvitin[30], O. I. Spiridonova[30], D. V. Oparin[30], V. Rumyantsev[31], O. A. Burkhonov[32], Sh. A. Egamberdiyev[32,33], V. Kim[34], M. Krugov[34], A. M. Tatarnikov[35], R. Inasaridze[36,37], Andrew J. Levan[4,38], Daniele Bjørn Malesani[24,25], Maria E. Ravasio[4,39], Jonathan Quirola-Vásquez[4], Joyce N. D. van Dalen[4], Javi Sánchez-Sierras[4], Daniel Mata Sánchez[40,41], Stuart P. Littlefair[42], Jennifer A. Chacón[43,44], Manuel A. P. Torres[40,41], Ashley A. Chrimes[4,45], Nikhil Sarin[46,47], Antonio Martin-Carrillo[48], Vik Dhillon[42], Yi Yang[49], Thomas G. Brink[10], Rebecca L. Davies[28], Sheng Yang[50], Amar Aryan[51], Ting-Wan Chen[51], Albert K. H. Kong[52], Wen-Xiong Li[1], Rui-Zhi Li[53,2], Jirong Mao[53,54,55], Ignacio Pérez-García[26], Emilio J. Fernández-García[26], Moira Andrews[56], Joseph Farah[56,57], Zhou Fan[1,2], Estefania Padilla Gonzalez[58], D. Andrew Howell[56,57], Dieter Hartmann[59], Jing-Wei Hu[1], Páll Jakobsson[60], Cheng-Kui Li[7], Zhi-Xing Ling[1,2], Curtis McCully[56,57], Megan Newsome[56,57], Benjamin Schneider[61,62], Kaew Samaporn Tinyanont[63], Ning-Chen Sun[1,2,15], Giacomo Terreran[64], Qing-Wen Tang[65], Wen-Xin Wang[1], Jing-Jing Xu[7], Wei-Min Yuan[1,2], Bin-Bin Zhang[8,6,9], Hai-Sheng Zhao[7], and Juan Zhang[7]

[1] National Astronomical Observatories, Chinese Academy of Sciences, Beijing 100101, People's Republic of China; dxu@nao.cas.cn
[2] School of Astronomy and Space Science, University of Chinese Academy of Sciences, Chinese Academy of Sciences, Beijing 100049, People's Republic of China
[3] Altay Astronomical Observatory, Altay, Xinjiang 836500, People's Republic of China
[4] Radboud University Nijmegen, Department of Astrophysics/IMAPP, P.O. Box 9010, Nijmegen, 6500 GL, The Netherlands
[5] Department of Astronomy, School of Physics, Huazhong University of Science and Technology, Wuhan, 430074, People's Republic of China; leiwh@hust.edu.cn
[6] Purple Mountain Observatory, Chinese Academy of Sciences, Nanjing 210023, People's Republic of China
[7] Key Laboratory of Particle Astrophysics, Institute of High Energy Physics, Chinese Academy of Sciences, Beijing 100049, People's Republic of China
[8] School of Astronomy and Space Science, Nanjing University, Nanjing 210093, People's Republic of China
[9] Key Laboratory of Modern Astronomy and Astrophysics (Nanjing University), Ministry of Education, People's Republic of China
[10] Department of Astronomy, University of California, Berkeley, CA 94720-3411, USA
[11] Space Research Institute, Russian Academy of Sciences, Profsoyuznaya ul. 84/32, Moscow, 117997, Russia
[12] National Research University "Higher School of Economics," Myasnitskaya ul. 20, Moscow, 101000, Russia
[13] Moscow Institute of Physics and Technology (MIPT), Institutskiy Pereulok, 9, Dolgoprudny, 141701, Russia
[14] School of Physics and Astronomy, Beijing Normal University, Beijing 100875, People's Republic of China
[15] Institute for Frontier in Astronomy and Astrophysics, Beijing Normal University, Beijing 102206, People's Republic of China
[16] Nevada Center for Astrophysics, University of Nevada Las Vegas, NV 89154, USA
[17] Department of Physics and Astronomy, University of Nevada Las Vegas, NV 89154, USA
[18] Astrophysics Research Institute, Liverpool John Moores University, IC2 Liverpool Science Park, 146 Brownlow Hill, Liverpool L3 5RF, UK
[19] University of Messina, MIFT Department, Via F.S. D'Alcontres 31, Messina, 98166, Italy
[20] Instituto de Alta Investigación, Universidad de Tarapacá, Casilla 7D, Arica, Chile
[21] Anton Pannekoek Institute of Astronomy, University of Amsterdam, Science Park 904, 1098 XH Amsterdam, The Netherlands
[22] Space Science Data Center (SSDC)—Agenzia Spaziale Italiana (ASI), I-00133 Roma, Italy
[23] Osservatorio Astronomico di Roma, via Frascati 33, I-00040 Monte Porzio Catone, Italy
[24] The Cosmic Dawn Centre (DAWN), Denmark
[25] Niels Bohr Institute, University of Copenhagen, Jagtvej 155, DK-2200, Copenhagen N, Denmark
[26] Instituto de Astrofísica de Andalucía (IAA-CSIC), Glorieta de la Astronomía s/n, 18008 Granada, Spain
[27] Ingeniería de Sistemas y Automática, Universidad de Málaga, Unidad Asociada al CSIC por el IAA, Escuela de Ingenierías Industriales, Arquitecto Francisco Peñalosa, 6, Campanillas, 29071 Málaga, Spain
[28] Center for Astrophysics and Supercomputing, Swinburne University of Technology, P.O. Box 218, Hawthorn, VIC 3122, Australia
[29] ARC Centre of Excellence for Gravitational Wave Discovery (OzGrav), Hawthorn, VIC 3122, Australia
[30] Special Astrophysical Observatory of the Russian Academy of Sciences, Nizhny Arkhyz 369167, Russia
[31] Crimean Astrophysical Observatory, 298409, Nauchny, Crimea[†]
[32] Ulugh Beg Astronomical Institute, Uzbek Academy of Sciences, Tashkent, Uzbekistan
[33] National University of Uzbekistan, Tashkent, Uzbekistan
[34] Fesenkov Astrophysical Institute, Almaty, 050020, Kazakhstan
[35] Sternberg Astronomical Institute, Lomonosov Moscow State University, Moscow, 119191, Russia
[36] Evgeni Kharadze Georgian National Astrophysical Observatory, 0301, Adigeni, Abastumani, Mt. Kanobili, Georgia
[37] Samtskhe-Javakheti State University, Rustaveli Str. 113, Akhaltsikhe, 0080, Georgia
[38] University of Warwick, Department of Physics, Coventry, CV4 7AL, UK
[39] Osservatorio Astronomico di Brera, Istituto Nazionale di Astrofisica, Merate 23807, Italy
[40] Instituto de Astrofísica de Canarias, E-38205, La Laguna, Tenerife, Spain
[41] Universidad de La Laguna, Departamento de Astroísica, E-38206, La Laguna, Tenerife, Spain
[42] University of Sheffield, Department of Physics and Astronomy, Sheffield, S3 7RH, UK
[43] Instituto de Astrofísica, Facultad de Física, Pontificia Universidad Católica de Chile, Campus San Joaquín, Av. Vicuña Mackenna 4860, Macul Santiago, 7820436, Chile
[44] Millennium Institute of Astrophysics, Nuncio Monseñor Sótero Sanz 100, Of 104, Providencia, Santiago, Chile
[45] European Space Agency (ESA), European Space Research and Technology Centre (ESTEC), Keplerlaan 1, Noordwijk, 2201 AZ, The Netherlands

[46] The Oskar Klein Centre, Department of Physics, Stockholm University, AlbaNova, Stockholm, SE-106 91, Stockholm, Sweden
[47] Nordita, Stockholm University and KTH Royal Institute of Technology, Hannes Alfvéns väg 12, Stockholm, SE-106 91, Stockholm, Sweden
[48] School of Physics and Centre for Space Research, University College Dublin, Dublin, D04 V1W8, Dublin, Ireland
[49] Physics Department, Tsinghua University, Beijing, 100084, People's Republic of China
[50] Institute for Gravitational Wave Astronomy, Henan Academy of Sciences, Zhengzhou 450046, Henan, People's Republic of China
[51] Graduate Institute of Astronomy, National Central University, 300 Jhongda Road, 32001 Jhongli, Taiwan
[52] Institute of Astronomy, National Tsing Hua University, No. 101 Sect. 2 Kuang-Fu Road, 30013 Hsinchu, Taiwan
[53] Yunnan Observatories, Chinese Academy of Sciences, Kunming 650216, People's Republic of China
[54] Center for Astronomical Mega-Science, Chinese Academy of Sciences, Beijing 100012, People's Republic of China
[55] Key Laboratory for the Structure and Evolution of Celestial Objects, Chinese Academy of Sciences, Kunming 650216, People's Republic of China
[56] Las Cumbres Observatory, 6740 Cortona Drive, Suite 102, Goleta, CA 93117-5575, USA
[57] Department of Physics, University of California, Santa Barbara, CA 93106-9530, USA
[58] Space Telescope Science Institute, 3700 San Martin Drive, Baltimore, MD 21218, USA
[59] Department of Physics and Astronomy, Clemson University, Clemson, SC 29631, USA
[60] Center for Astrophysics and Cosmology, Science Institute, University of Iceland, Dunhagi 5, 107 Reykjavík, Iceland
[61] Massachusetts Institute of Technology, Kavli Institute for Astrophysics and Space Research, Cambridge, MA, USA
[62] Aix Marseille Université, CNRS, CNES, LAM, Marseille, France
[63] National Astronomical Research Institute of Thailand, 260 Moo 4, T. Donkaew, A. Maerim, Chiangmai, 50180, Thailand
[64] Adler Planetarium, 1300 South DuSable Lake Shore Drive, Chicago, IL 60605, USA
[65] Department of Physics, School of Physics and Materials Science, Nanchang University, Nanchang 330031, People's Republic of China
Received 2025 March 6; revised 2025 May 23; accepted 2025 May 30; published 2025 July 17

Abstract

We present multiband observations and analysis of EP240801a, a low-energy, extremely soft gamma-ray burst (GRB) discovered on 2024 August 1 by the Einstein Probe (EP) satellite with a weak contemporaneous signal also detected by the Fermi Gamma-ray Burst Monitor (GBM). Optical spectroscopy of the afterglow, obtained by Gran Telescopio Canarias and Keck, identified the redshift of $z = 1.6734$. EP240801a exhibits a burst duration of 148 s in X-rays and 22.3 s in gamma rays, with X-rays leading by 80.61 s. Spectral lag analysis indicates that the gamma-ray signal arrived 8.3 s earlier than the X-rays. Joint spectral fitting of EP Wide-field X-ray Telescope and Fermi/GBM data yields an isotropic energy $E_{\gamma,\rm iso} = (5.57^{+0.54}_{-0.50}) \times 10^{51}$ erg, a peak energy $E_{\rm peak} = 14.90^{+7.08}_{-4.71}$ keV, and a fluence ratio $S(25\text{–}50\,\rm keV)/S(50\text{–}100\,\rm keV) = 1.67^{+0.74}_{-0.46}$, classifying EP240801a as an X-ray flash (XRF). The host-galaxy continuum spectrum, inferred using `Prospector`, was used to correct its contribution for the observed outburst optical data. Unusual early *R*-band behavior and EP Follow-up X-ray Telescope observations suggest multiple components in the afterglow. Three models are considered: a two-component jet model, a forward-reverse shock model, and a forward shock model with energy injection. All three provide reasonable explanations. The two-component jet model and the energy injection model imply a relatively small initial energy and velocity of the jet in the line of sight, while the forward-reverse shock model remains typical. Under the two-component jet model, EP240801a may resemble GRB 221009A (BOAT) if the bright narrow beam is viewed on-axis. Therefore, EP240801a can be interpreted as an off-beam (narrow) jet or an intrinsically weak GRB jet. Our findings provide crucial clues for uncovering the origin of XRFs.

Unified Astronomy Thesaurus concepts: Gamma-ray bursts (629); X-ray transient sources (1852)

1. Introduction

Gamma-ray bursts (GRBs) are extraordinarily energetic and luminous catastrophic events in the Universe, with a typical isotropic energy of 10^{50}–10^{55} erg released in the prompt emission phase (J. L. Atteia et al. 2017). The duration of GRBs (T_{90}, defined as the time span from 5% to 95% of the total prompt emission fluence) typically ranges from subseconds to several thousand seconds (P. Kumar & B. Zhang 2015). The statistics of the duration of the GRB prompt emission T_{90} reveal two primary types of GRB (C. Kouveliotou et al. 1993; B. Zhang et al. 2009): type I bursts (most with $T_{90} < 2$ s, so they are also called "short GRBs") and type II bursts (most with $T_{90} > 2$ s, known as "long GRBs"). From the 1234 BATSE GRB samples[66] (W. S. Paciesas et al. 1999), type II bursts constitute about 70% of the total GRB sample, originate from the collapse of massive stars, and are associated with broad-line Type Ic supernovae (T. J. Galama et al. 1999; S. E. Woosley & J. S. Bloom 2006; P. Kumar & B. Zhang 2015). In contrast, about 30% of the GRBs are classified as type I bursts, which originate from compact star mergers and are accompanied by kilonovae (C. Kouveliotou et al. 1993; B. Zhang et al. 2009; B. P. Abbott et al. 2017). However, there are some exceptions, e.g., long-duration type I and short-duration type II GRBs such as GRB 060505 (J. P. U. Fynbo et al. 2006), GRB 060614 (M. Della Valle et al. 2006; J. P. U. Fynbo et al. 2006; N. Gehrels et al. 2006; B. Yang et al. 2015), GRB 200826A (T. Ahumada et al. 2021; B. B. Zhang et al. 2021), GRB 211221A (J. C. Rastinejad et al. 2022; E. Troja et al. 2022), and GRB 230307A (A. J. Levan et al. 2024; Y.-H. Yang et al. 2024).

As extensions of the classical GRBs (C-GRBs), there are some fainter events, e.g., low-luminosity GRBs (i.e., T. J. Galama et al. 1998; S. Y. Sazonov et al. 2004;

[†] While the AAS journals adhere to and respect UN resolutions regarding the designations of territories (available at http://www.un.org/press/en), it is our policy to use the affiliations provided by our authors on published articles.

[66] https://gammaray.msfc.nasa.gov/batse/grb/catalog/4b/index.html

S. Campana et al. 2006), X-ray-rich GRBs (XRRs; see T. Sakamoto et al. 2008), and X-ray flashes (XRFs; see C. Barraud et al. 2003), whose physical origins remain a mystery. Possible scenarios include off-axis GRBs (e.g., R. Yamazaki et al. 2002; Y. Urata et al. 2015), structured jets (e.g., Y. Sato et al. 2021), dirty jets, and shock breakout of a mildly relativistic jet.

The Einstein Probe (EP), launched on 2024 January 9, is dedicated to monitoring the soft X-ray sky (W. Yuan et al. 2025). The satellite is equipped with a Wide-field X-ray Telescope (WXT; 0.5–4 keV; W. Yuan et al. 2022) and a Follow-up X-ray Telescope (FXT; 0.3–10 keV; Y. Chen et al. 2020). The WXT's lobster-eye micropore optics provide an expansive field of view of $\sim$3600 deg^2 with a sensitivity of $\sim 2.6 \times 10^{-11}$ erg s^{-1} cm^{-2} in 0.5–4 keV with 1 ks exposure, which is a significant advantage for detecting transients in space. The autonomous follow-up observations by FXT provide quick positions accurate to $\sim 10''$. Thanks to the high sensitivity and wide-field monitoring in soft X-rays, EP is efficient in detecting weak GRBs, providing a great opportunity to unveil the physics behind.

In this Letter, we present an extremely soft GRB detected by EP/WXT, EP240801a, and analyze and discuss the mechanism of the burst in detail. EP/WXT detected EP240801a with an uncertainty of $\sim 3'$, and EP/FXT rapidly performed a follow-up observation $\sim$180 s later, which reduced the positional uncertainty to $\sim 10''$ (H. Zhou et al. 2024). As a result, the field of EP240801a was observed in multiple bands, and a spectroscopic redshift of EP240801a was discovered soon after the trigger (S. Y. Fu et al. 2024a; J. Quirola-Vásquez et al. 2024; W. Zheng et al. 2024). The observed data collected from several facilities are introduced in Section 2. Section 3 presents our analysis of the prompt emission phase, afterglow phase, and host galaxy. In Sections 4 and 5, we respectively discuss the models of EP240801a and summarize our work. The conventional cosmological model we adopted is as follows: $H_0 = 69.6$ km s^{-1} Mpc^{-1}, $\Omega_M = 0.286$, $\Omega_\Lambda = 0.714$ (C. L. Bennett et al. 2014).

2. Observations and Data Reduction

2.1. EP Observations

EP240801a has an unabsorbed peak flux $(3.10 \pm 0.64) \times 10^{-8}$ erg s^{-1} cm^{-2} in 0.5–4 keV, and it is located at R.A. $= 345.^\circ1630$, decl. $= 32.^\circ5927$ (J2000) with an uncertainty of $10''$ in radius (at 90% confidence, statistical and systematic). FXT performed six more follow-up observations until 6.5 days after the burst, and EP240801a was identified in the first four of those observations.

The processing and calibration of WXT photon events are handled by adopting specialized data reduction software and the calibration database (Y. Liu et al. 2025, in preparation). The calibration database is generated on the basis of the results of the on-ground calibration experiments (H.-Q. Cheng et al. 2025). The position of each photon was converted to celestial coordinates (J2000). The energy value of each event is calculated according to the bias and gain stored in the calibration database. After bad/flaring pixels were flagged, single, double, triple, and quadruple events without anomalous flags were selected to form the cleaned event file. The photons of the source and the background were extracted from a circle with a radius of $9'$ and an annulus with radii of $18'$ and $36'$, respectively. As the WXT average net count rate is $\sim$2.9 in the total prompt emission phase, we grouped the WXT data with 5 minimum counts per bin to perform the spectral analysis.

The FXT cleaned event files and response files were generated by using the Follow-up X-ray Telescope Data Analysis Software (`FXTDAS v1.10`).[67] The process involved particle event identification, pulse invariant conversion, grade calculation and selection (grade $\leqslant 12$), bad- and hot-pixel flagging, and selection of good time intervals using a housekeeping file. With 90% of the point-spread function enclosed by an $a \sim 1'$ radius circle at 1.5 keV, the photons of the source and background were extracted from a circle with a radius of $1'$ and an annulus with radii of $2'$ and $3'$, respectively. The FXT data at various times were also grouped with different counts to enhance the signal-to-noise ratio (SNR).

After reprocessing the WXT data, the start time of EP240801a was determined to be 09:06:20.7 on 2024 August 1 (hereafter T_0; UTC dates are used throughout this Letter) by using the Bayesian block method (J. D. Scargle et al. 2013) with a false-alarm probability of $p_0 = 0.005$. This probability yields a conservative estimate that is suited to the characteristics of the WXT data. T_0 is 17.7 s later than the start time reported by H. Zhou et al. (2024) in the General Coordinates Network (GCN) circular. The prompt emission shows a multipeaked structure as illustrated in Figure 1. Spectral analysis was performed with `Xspec v12.14.0h` (K. A. Arnaud 1996) for EP data; details can be seen in Section 3.1.2. The results of the EP observations are presented in Table 1.

2.2. Fermi Observations

Based on the trigger time and location of the burst, we found a weak, subthreshold signal 80.61 s after T_0 by using the Bayesian block method in the archival data of the Gamma-ray Burst Monitor (GBM; C. Meegan et al. 2009) on board the Fermi Gamma-Ray Space Telescope (Fermi). This signal was detected in the four closest detectors (n6, n7, n9, and nb) of GBM. By fitting a first-order polynomial to the GBM data before and after the signal (i.e., -100 to 70 s and 150–200 s referenced to T_0, respectively), we eliminated the background contribution, providing the background-subtracted gamma-ray light curve, as depicted in Figure 1.

Spectral analysis was conducted using the four closest sodium iodide (Na I; 8 keV–1 MeV) detectors. The two bismuth germanate (200 keV–40 MeV) detectors were excluded from the spectral analysis due to the absence of significant transient signals in their data. We excluded the GBM data between 30 keV and 40 keV (corresponding to the iodine K-edge; see C. Meegan et al. 2009) and the channels at the extremes of the spectra (channels below 8 keV and channels 127 and 128 for Na I). We obtained the time-tagged event data covering the time range of EP240801a from the Fermi/GBM public data archive.[68] `The Multi-Mission Maximum Likelihood Framework` (`threeML`; G. Vianello et al. 2015) is the main tool for analysis of Fermi/GBM data.

[67] http://epfxt.ihep.ac.cn/analysis
[68] https://heasarc.gsfc.nasa.gov/FTP/fermi/data/gbm/daily/

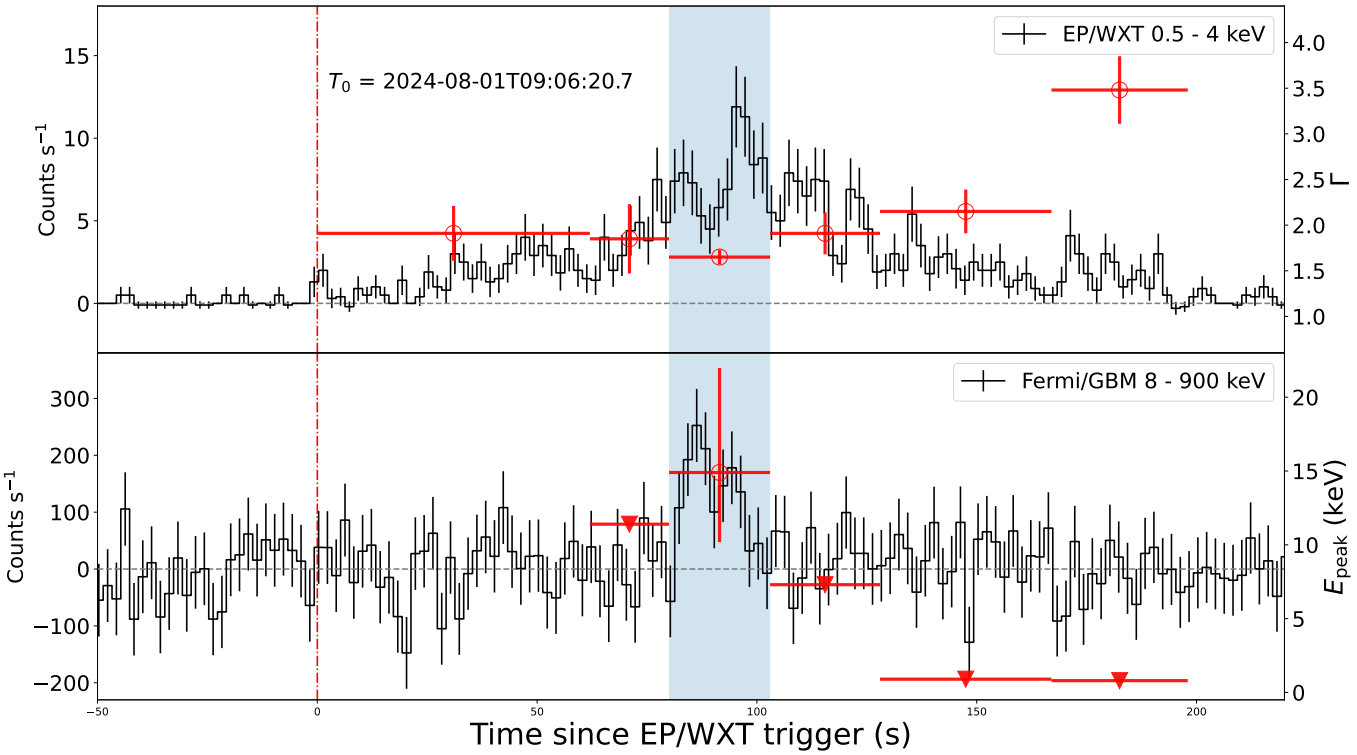

Figure 1. The prompt emission light curve obtained by EP/WXT and Fermi/GBM; the gray dotted lines indicate zero count rate. The red dashed–dotted line represents the T_0 of EP240801a, and the UTC time is indicated. We analyzed the joint spectrum of EP/WXT and Fermi/GBM data during the vertical light blue slice. The photon index (red circles) of the time-resolved fit of the EP/WXT data is shown in the upper panel. The lower panel depicts the E_{peak} of EP240801a, and the inverted triangle symbols signify limits.

2.3. Ground-based Observations

The optical counterpart of EP240801a was first detected by the 0.7 m telescope of the Thai Robotic Telescope (TRT) network at 11:06:18 on 2024 August 1, 2.24 hr after the EP/WXT trigger. It was located at (J2000) R.A. $= 23^{\rm h}00^{\rm m}39\overset{\rm s}{.}03$, decl. $= +32^{\circ}35'37\overset{''}{.}95$ with an uncertainty of $0\overset{''}{.}5$; this is $4\overset{''}{.}4$ away from the FXT center position (S. Y. Fu et al. 2024a). The celestial location of the burst is shown in Figure 2. The follow-up observations have been performed by a considerable number of ground-based telescopes. Details of the filters used with the telescopes, along with the photometric results, are presented in Table A1 and described in Section 3.2.1. The photometric methods are described in Appendix B.

2.4. Optical Spectroscopy

The optical spectra of EP240801a were obtained with the Optical System for Imaging and low-intermediate-Resolution Integrated Spectroscopy (OSIRIS+) instrument mounted on the 10.4 m Gran Telescopio Canarias (GTC; J. Cepa et al. 2000) at ∼0.79 days after the EP/WXT trigger time with an exposure time of 4 × 1200 s (J. Quirola-Vásquez et al. 2024) and the Low Resolution Imaging Spectrometer (LRIS) mounted on the Keck telescope (J. B. Oke et al. 1995) at ∼1.02 days with an exposure time of 3 × 950 s (W. Zheng et al. 2024); see details in Appendix B.

The sections of the spectra with the highest SNR (6000–8500 Å) are illustrated in Figure 3. The significant Mg II doublet and some Fe II absorption lines lead to a redshift of $z = 1.6734 \pm 0.0002$. Hence, we consider this value as the redshift of EP240801a, based on the reasonable assumption that the transient occurred in the galaxy producing those lines rather than one at a greater distance.

3. Results

3.1. Prompt Emission

3.1.1. Light Curve

In Figure 1, we present the prompt emission light curves of EP240801a with EP/WXT data at 0.5–4 keV and Fermi/GBM data at 8–900 keV, both with 2 s bin size. The prompt emission shows multiple pulses at 0.5–4 keV with $T_{90} = 148.0 \pm 3.2$ s. Only two peaks within $T_{90} = 22.30 \pm 9.92$ s are visible at 8–900 keV in the light curve from Fermi/GBM data. The spectral lag of EP/WXT and Fermi/GBM data was calculated by using the cross-correlation function (D. L. Band 1997; J. P. Norris et al. 2000; T. N. Ukwatta et al. 2010) method with a 500 ms time bin. For the uncertainty of the lags, we used the Monte Carlo simulation (see B. M. Peterson et al. 1998; T. N. Ukwatta et al. 2010). The lag value is 8.3 ± 0.8 s, which indicates that the gamma-ray signal arrived 8.3 s earlier.

3.1.2. Analysis of the High-energy Spectra

We perform X-ray data analyses via `Xspec` and employ `threeML` for gamma-ray data and joint fitting. The absorbed power-law model *zTbAbs* × *TbAbs* × *PowerLaw* was used to fit the X-ray spectra. The first and second components are responsible for the intrinsic absorption and the Galactic absorption using the Tüebingen–Boulder interstellar medium (ISM) absorption model (J. Wilms et al. 2000). For the Galactic hydrogen column density, we adopt $N_{\rm H} = 9.78 \times$

Table 1
Spectral Fitting Results and Corresponding Fitting Statistics for EP and Fermi/GBM

Time Intervals (s)	Instruments	Intrinsic Absorption (cm^{-2})	Photon Index[a] (Γ)	E_{peak}[b] (keV)	STAT/(d.o.f.)[c]
0–198	WXT	$(2.13 \pm 0.54) \times 10^{22}$	1.99 ± 0.18	⋯	79.73/83
0–62		–	1.91 ± 0.30	⋯	8.84/14
62–80		–	1.85 ± 0.38	<11.4	24.86/20
80–103	WXT+GBM	–	1.65 ± 0.08	$14.90^{+7.08}_{-4.71}$	(46.70+154.40)/205
103–128	WXT	–	1.91 ± 0.23	<7.3	46.54/46
128–167		–	2.15 ± 0.24	<0.9	44.16/51
167–198		–	3.48 ± 0.37	<0.8	24.10/30
232–697	FXT	$<0.07 \times 10^{22}$	3.29 ± 0.07	⋯	62.13/53
3.75×10^3–6.30×10^3		$(0.56 \pm 0.45) \times 10^{22}$	2.18 ± 0.15	⋯	24.79/33
1.54×10^5–1.41×10^6		$<1.11 \times 10^{22}$	$1.73^{+0.28}_{-0.15}$	⋯	59.77/49

Notes. Dashes (–) in the Intrinsic Absorption column indicate that we use the same value as the result above. All error bars represent 1σ uncertainties.
[a] An absorbed power-law model (*zTbAbs* × *TbAbs* × *PowerLaw*) is used to fit the X-ray data, and the Galactic hydrogen column density is fixed with $N_H = 9.78 \times 10^{20}\,cm^{-2}$. When GBM data are involved, *PowerLaw* is replaced by *Cutoff* − *PowerLaw*.
[b] The upper limits of E_{peak} are derived from either the GBM upper limits or the WXT data and are independent of the fitting process. For further details, see Section 3.1.2.
[c] We use PGSTAT for GBM data and CSTAT for EP/WXT and EP/FXT data.

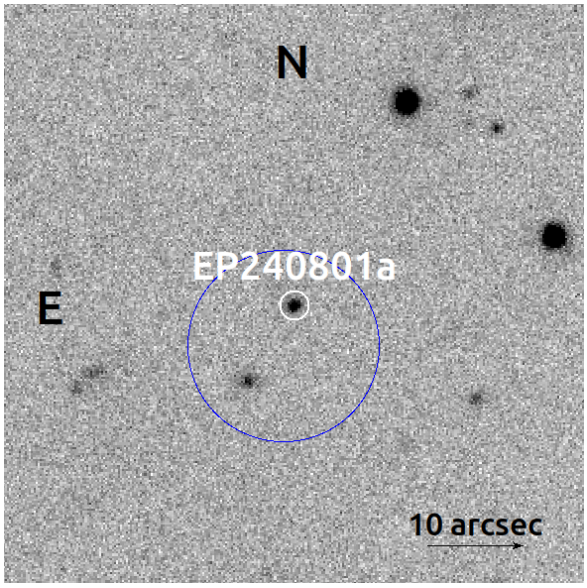

Figure 2. The Sloan r'-band position of EP240801a with the field of view of $1' \times 1'$ obtained by NOT/ALFOSC about 0.8 days after the discovery of EP240801a. The location of the burst is circled in white, and the $10''$ error circle of EP/FXT is in blue.

$10^{20}\,cm^{-2}$ throughout this Letter, as calculated by the UK Swift Science Data Centre[69] using the method described in R. Willingale et al. (2013). The third component is a simple photon power law, with $N(E) = K\left(\frac{E}{1\,keV}\right)^{-\Gamma}$, where K is the normalization of the spectrum and Γ is the dimensionless photon index of the power law. The cutoff power-law model proves to be more suitable for the GBM spectrum and the X-ray/gamma-ray joint fit of EP240801a, as its results have a lower Bayesian information criterion (BIC; G. Schwarz 1978; A. R. Liddle 2007) value compared to the Band models'. Thus, we used the cutoff power-law model $N(E) = K\left(\frac{E}{100\,keV}\right)^{-\Gamma}\exp^{-\frac{E}{E_c}}$, where K is the normalization of the spectrum, Γ is the dimensionless photon index, and $(2-\Gamma)E_c$ represents the peak energy E_{peak} of the νF_ν spectrum, to analyze the WXT and GBM data during the light blue slice in Figure 1, assuming the Galactic absorption and intrinsic absorption as derived from the EP/WXT analysis before; see Figure 4. The fitting results and the corresponding statistics for each time interval are listed in Table 1. We used CSTAT (W. Cash 1979) for EP data and PGSTAT (K. A. Arnaud 1996) for Fermi/GBM data.

For those time periods without GBM signals, we use the 3σ upper limits from GBM data with a 16 s timescale to constrain E_{peak}. We assumed that the power-law model evolves into a cutoff power-law model as the energy reaches higher. In doing so, the photon index and normalization of the cutoff power-law model are taken to be the same as those in the original power-law model. Consequently, E_{peak} can be constrained with the nondetection results of GBM data. There are certain time intervals, such as 0–62 s and 128–198 s, where the GBM upper limits are too high to constrain E_{peak}. However, for the interval 128–198 s, we can constrain E_{peak} using WXT data due to its softer spectral index. The soft spectrum indicates that E_{peak} lies near or below 0.5 keV, the lower energy bound of WXT. We performed spectral fitting with an absorbed broken power-law model to better constrain its peak energy. The low-energy photon index was fixed to be 1, a typical value for GRBs, while the intrinsic absorption and Galactic absorption were fixed to those in WXT spectral analysis before. Thus, a conservative upper limit can be derived.

The fitting results in differential phases were used to obtain the X-ray flux density at 1 keV, as shown in Section 3.2.1. The spectral evolution of EP/WXT data, as illustrated in Figure 1, indicates that the spectrum initially hardens and then softens, with EP240801a being detected by Fermi/GBM at its hardest stage. We find $E_{\gamma,iso} = (5.57^{+0.54}_{-0.50}) \times 10^{51}$ erg in 1–10^4 keV in the rest frame, $E_{peak} = 14.90^{+7.08}_{-4.71}$ keV, and the fluence ratio $S(25-50\,keV)/S(50-100\,keV) = 1.67^{+0.74}_{-0.46}$ for EP240801a. The parameters above are shown in Figures 5 and 6. As described by T. Sakamoto et al. (2008), the empirical

[69] https://www.swift.ac.uk/analysis/nhtot/

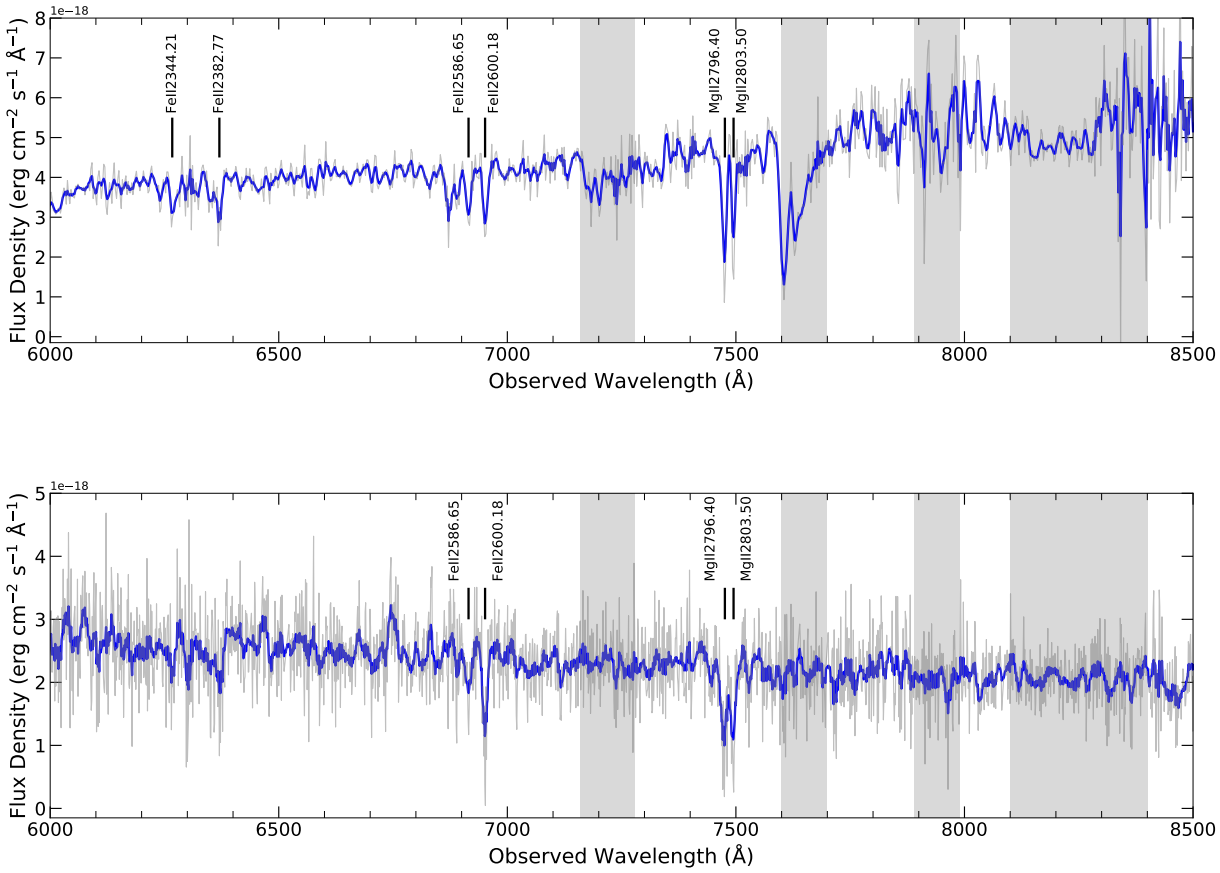

Figure 3. The spectrum obtained with GTC/OSIRIS+ (top panel) and Keck/LRIS (bottom panel). The gray line represents the raw spectrum, while the blue line has been smoothed for display purposes. The identified metal absorption lines are indicated with vertical dashes, and the gray vertical bands indicate the locations of telluric features. From the observed absorption lines, especially Mg II $\lambda\lambda$2796, 2803 and Fe II λ2600, we determine $z = 1.6734 \pm 0.0002$ for EP240801a, assuming the transient occurred in the host galaxy at that redshift.

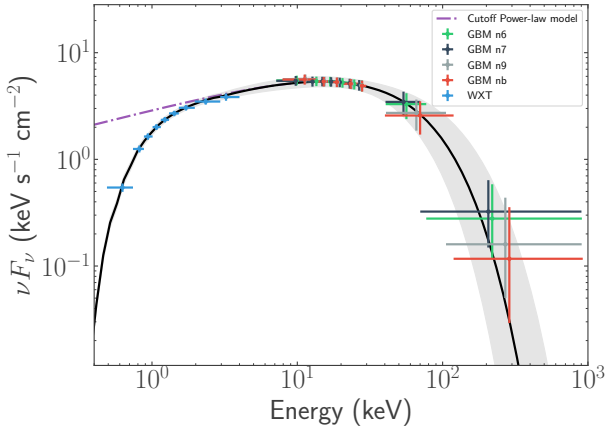

Figure 4. The spectral joint fitting of EP/WXT and Fermi/GBM data during the light blue slice in Figure 1. The black solid line represents the best-fit absorbed cutoff power-law model, and the shadow is the 1σ uncertainty interval, while the violet dashed–dotted line shows the individual cutoff power-law model. The data from different detectors are marked as various colors.

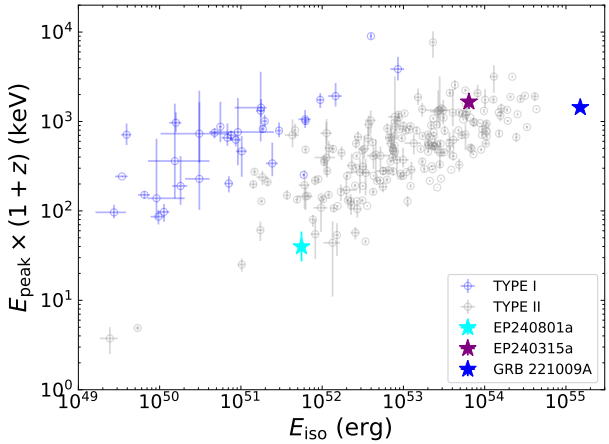

Figure 5. Amati diagram of EP240801a (cyan star); the blue and gray circles represent other type I and type II GRBs, respectively. Another GRB detected by EP, EP240315a, is marked as a purple star. GRB 221009A is marked as a blue star.

definitions of XRFs, XRRs, and C-GRBs are as follows:

$$S(25\text{–}50\,\mathrm{keV})/S(50\text{–}100\,\mathrm{keV}) \leqslant 0.72 \quad (\mathrm{C-GRBs}),$$
$$0.72 < S(25\text{–}50\,\mathrm{keV})/S(50\text{–}100\,\mathrm{keV}) \leqslant 1.32 \quad (\mathrm{XRRs}),$$
$$1.32 < S(25\text{–}50\,\mathrm{keV})/S(50\text{–}100\,\mathrm{keV}) \quad (\mathrm{XRFs}).$$

Thus, EP240801a is classified as an XRF. Despite this classification as an XRF, some $\sim$100 keV photons are detected. The statistical properties of EP240801a are consistent with the XRFs in the third Swift Burst Alert Telescope catalog, as indicated in X. Bi et al. (2018), suggesting a greater likelihood of association with a supernova explosion.

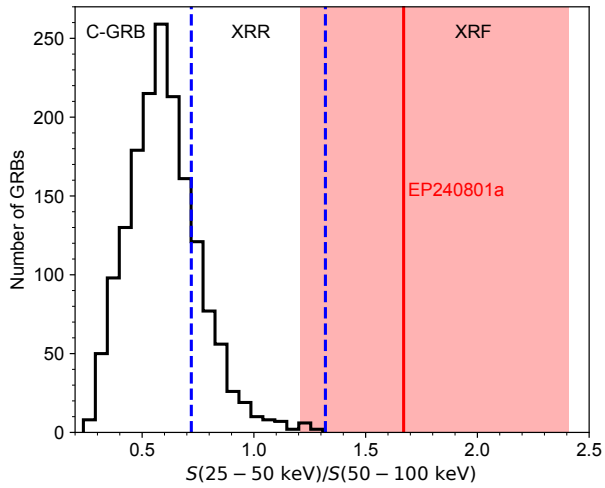

Figure 6. The fluence ratio $S(25–50\,\mathrm{keV})/S(50–100\,\mathrm{keV})$ of 1647 GRBs recorded in the Fermi/GBM archive from 2008 to 2020; most of them are C-GRBs due to the higher trigger threshold of Fermi/GBM for the soft events. The red line represents the fluence ratio of EP240801a, and the shadow is the 1σ uncertainty interval. The blue dashed lines represent the boundaries of C-GRBs, XRRs, and XRFs described by T. Sakamoto et al. (2008).

3.2. Afterglow Emission

3.2.1. Light Curve

The X-ray, near-infrared (NIR), and optical data from the prompt to afterglow phases are illustrated in Figure 7. The EP/WXT and EP/FXT data during the prompt phase are shown in the inset. The optical and NIR light curves obtained from ∼0.02 to ∼13.78 days include the u', g', r', i', z', B, V, R, I, J, and H bands. The light curve in the afterglow phase can be divided into two parts. The initial data set comprises a seemingly shallow decay phase occurring between ∼1 and 9 ks. Its flux density exhibits a shallow decay index $\alpha = 0.25 \pm 0.05$ for X-ray and R-band data, as derived from a single power-law model $F \propto t^{-\alpha}$, and may imply complex jet emission components, namely, a structured jet, a reverse shock (RS) along with a forward shock (FS), or an energy injection scenario. The light curve at later times exhibits a normal decay with $\alpha = 0.95 \pm 0.03$, as obtained by fitting the r'-, R-, and X-ray-band data, which is consistent with the predicted value of $\alpha \sim 1$ from the standard external FS model (B. Zhang 2018).

3.2.2. Afterglow Spectral Energy Distribution Analysis

A spectral energy distribution (SED) analysis enables a deeper understanding of the afterglow evolution. We conducted an SED analysis at ∼70 ks, denoted by the light blue region in Figure 7. The optical data in the Sloan g', r', i', z' bands obtained from the Alhambra Faint Object Spectrograph and Camera (ALFOSC) mounted on the 2.56 m Nordic Optical Telescope (NOT) and the X-ray data deduced from later times using the temporal decay index $\alpha = 0.95$ were used for the SED; see Figure 8. We fit the spectrum with a power-law function from the *zDust* × *zTbAbs* × *TbAbs* × *PowerLaw* model in `Xspec v12.14.0h`, where *zdust* represents extinction by dust grains in the host galaxy of the burst and *zTbAbs* and *TbAbs* are, respectively, the intrinsic hydrogen photoelectric absorption in the host galaxy and the Milky Way. The redshift and the Galactic hydrogen column density are fixed to 1.6734 and $N_{\rm H} = 9.78 \times 10^{20}\,\mathrm{cm}^{-2}$, respectively. For all three extinction laws (Milky Way, Large Magellanic Cloud, or Small Magellanic Cloud), the $E(B-V)$ of the host galaxy cannot be accurately constrained and tends toward zero under the optimal statistical conditions. The best-fitting result gives the spectral index $\beta = 0.69 \pm 0.02$ in the optical to X-ray bands.

3.3. Host Galaxy

A faint source located at (J2000) R.A. $= 23^{\rm h}00^{\rm m}39\overset{\rm s}{.}02$, decl. $= +32°35'37\overset{''}{.}45$, which is $\sim 0\overset{''}{.}56$ away from the position of EP240801a, was detected in archival observations in the Legacy Surveys. According to the Legacy Surveys' result, the photometric redshift of this source is 0.99 ± 0.35 (R. Zhou et al. 2021). We calculated the chance alignment probability that one source as bright as or brighter than this galaxy within this offset is found in the GTC/HiPERCAM r'-band image. We obtained $P_{\rm chance} = 0.002$ for this galaxy. Hence, it is likely that this is indeed the host galaxy of EP240801a. Photometry of the host galaxy in the g', r', i', z', J, Ks bands was recently obtained from GTC, NOT, SAI-25, and the 8.2 m Very Large Telescope (VLT) as listed in Table A1. We took the u'- and H-band last detections by GTC as the upper limits of the host galaxy. We searched the catalogs and images in the Galaxy Evolution Explorer (GALEX) All-Sky Survey and the Wide-field Infrared Survey Explorer final catalog (AllWISE) and calculated the 5σ upper limits of these previous observations from the known sources in their catalogs or images to obtain the multiband photometry of the host galaxy. To investigate the stellar population properties of the host, we utilized `Prospector` (B. D. Johnson et al. 2021) to fit the host photometry; see Figure 9. Consequently, we presented all the observed data corrected for the host-galaxy contributions in Figure 7. The magnitudes of the host galaxy and the details are presented in Table 2 and Appendix C.

3.4. Closure Relations

For the time period we are interested in (the first few days), the jet might enter the deceleration phase (R. Sari et al. 1998). The temporal decay index $\alpha = 0.95 \pm 0.03$ and the spectral index $\beta = 0.69 \pm 0.02$ suggest that the frequencies of optical and X-ray emissions may lie between the minimum injection frequency ν_m and the synchrotron cooling frequency $\nu_{\rm c}$, namely, $\nu_m < \nu_{\rm optical} < \nu_{\rm X\text{-}ray} < \nu_c$. According to the closure relation (B. Zhang & P. Mészáros 2004; H. Gao et al. 2013), the electron energy distribution index p is expected with $\beta = (p-1)/2$. As $p = 2.38 \pm 0.04$ derived from β, we have the temporal decay index α in a self-similar deceleration phase for $\nu_{\rm a} < \nu_{\rm m} < \nu < \nu_{\rm c}$ and $p > 2$ with

$$F_\nu \propto \begin{cases} t^{-\frac{3(p-1)}{4}} & \text{ISM} \\ t^{-\frac{3p-1}{4}} & \text{Wind} \end{cases}. \quad (1)$$

This corresponds to $\alpha_{\rm ISM} = 1.035 \pm 0.03$ and $\alpha_{\rm Wind} = 1.535 \pm 0.03$. Thus, the wind case is disfavored for EP240801a. Nevertheless, the wind scenario remains plausible, especially if it evolves from an early wind-dominated environment to a constant-density ISM environment (R. A. Chevalier et al. 2004), as the time of the SED is at the late-time phase.

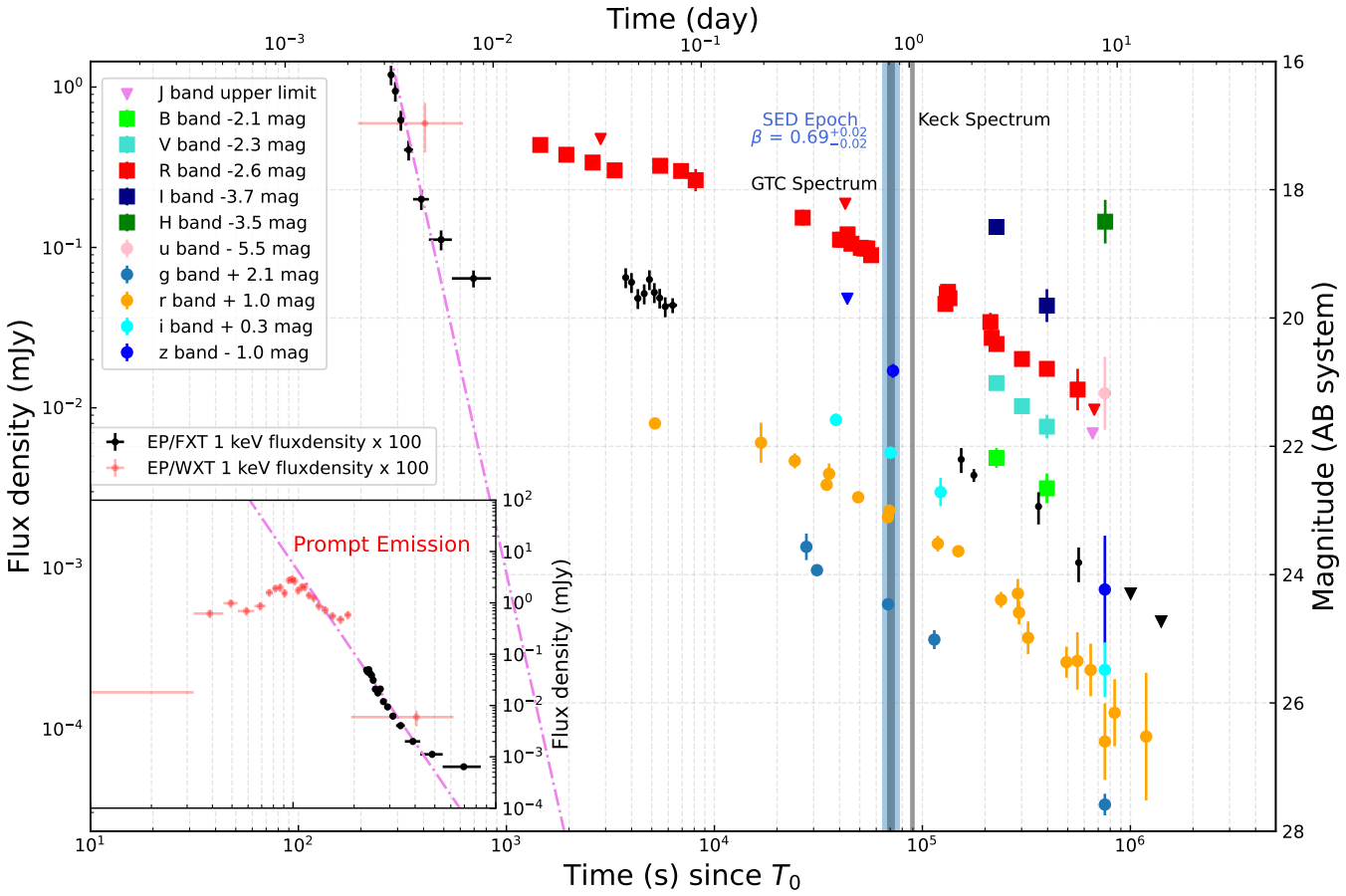

Figure 7. Light curves of EP240801a from the prompt phase to the afterglow phase in X-rays, optical, and NIR. The EP/WXT (red circles) and EP/FXT (black circles) data are presented with unabsorbed flux density at 1 keV and scaled by a factor of 100 in the main figure but not scaled in the inset. The inset shares the time axis with the main figure. The optical/NIR data are in the AB system (J. B. Oke & J. E. Gunn 1983) and have been corrected for Galactic extinction, which is $E(B-V) = 0.093$ mag (E. F. Schlafly & D. P. Finkbeiner 2011), and the host-galaxy magnitude. All the inverted triangle symbols signify limits. The light blue slice represents the time of the SED. Two gray slices represent the time of the GTC and the Keck optical spectrum, respectively. A violet dashed–dotted single power law with $\alpha = 5.82 \pm 0.32$ is depicted in both the main figure and the inset.

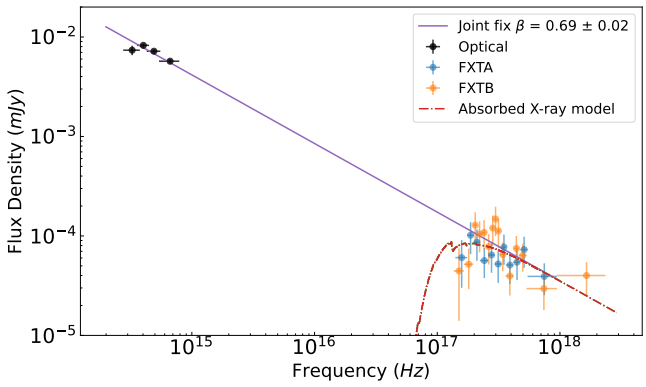

Figure 8. The afterglow SED of EP240801a at 70 ks from optical to X-ray frequencies. The optical multiband data are listed in Table A1. The violet line represents the result of a single power-law fit with $\beta = 0.69 \pm 0.02$. The dashed–dotted red line represents the X-ray fit.

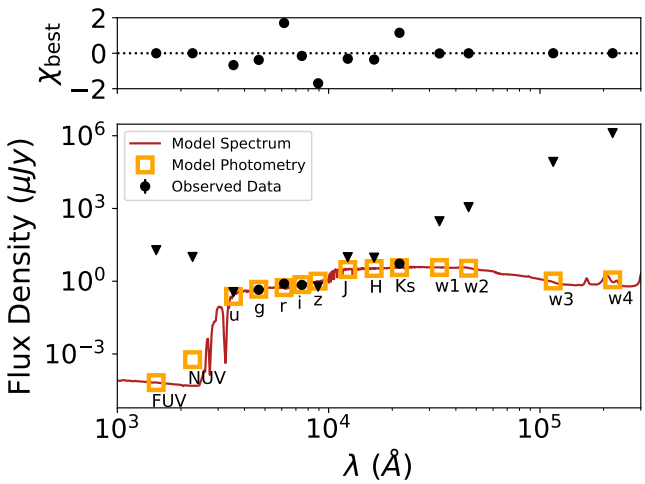

Figure 9. SED of the host galaxy of EP240801a. The best-fit model SED is shown by the red line. χ_{best} means a standardized residual. The model photometry results are marked as squares with their corresponding bands below, and the observed data are indicated by black data points (black inverted triangles represent upper limits). All the data are corrected for Galactic extinction.

4. Theoretical Interpretation and Discussion

As discussed in Section 3.2.1 and illustrated in Figure 7, the afterglow light curve (X-ray, NIR, and optical) can be divided into two parts: a shallow decay phase occurring between ∼1 and 9 ks with $\alpha = 0.25 \pm 0.05$ for X-ray and R-band data and a normal decay at later times with $\alpha = 0.95 \pm 0.03$ as obtained by fitting the r'-, R-, and X-ray-band data. These distinct behaviors disfavor the interpretation with a single FS model.

Table 2
Host-galaxy Magnitudes of EP240801a

Band	Magnitude (AB)	References
FUV	>20.70	GALEX
NUV	>21.40	GALEX
u	>25.48	GTC
g	25.13 ± 0.11	GTC
r	24.40 ± 0.19	NOT
i	24.46 ± 0.20	NOT
z	>24.60	GTC
J	>21.80	SAI-25
H	>21.52	GTC
Ks	22.12 ± 0.29	VLT
*W*1	>17.74	AllWISE
*W*2	>16.28	AllWISE
*W*3	>11.60	AllWISE
*W*4	>8.63	AllWISE
u	25.92 ± 0.25	`Prospector` model results
z	24.03 ± 0.25	`Prospector` model results
B	25.22 ± 0.25	`Prospector` model results
V	24.86 ± 0.25	`Prospector` model results
R	24.71 ± 0.25	`Prospector` model results
I	24.27 ± 0.25	`Prospector` model results
H	22.64 ± 0.25	`Prospector` model results

To understand the two different afterglow epochs of EP240801a, we consider three models, i.e., a two-component jet model, a reverse-forward shock model, and an FS model with energy injection.

We employ the numerical code `PyFRS`[70] to calculate the RS and FS emissions (H. Gao et al. 2013; B. Zhang 2018; Z.-P. Zhu et al. 2023; S.-Y. Fu et al. 2024b; C. Zhou et al. 2024). We use the top-hat jet type in the modeling. Markov Chain Monte Carlo (MCMC) with `PyFRS` is adopted for multiband fitting to place constraints on the model parameters. The MCMC fit is performed using the Python package `emcee` (D. Foreman-Mackey et al. 2013), which utilizes a group of parallel-tempered affine invariant walkers to explore the parameter space. A general description of the afterglow model and the details of the fitting are presented in Appendix D. The best-fitting light curve and the posterior probability distributions with 1σ uncertainties of the parameters are illustrated in Figure 10 and listed in Table 3, respectively. As we can see, all three models can generally reproduce the multiband afterglow observations. We will discuss the fit results in the following subsections.

4.1. Two-component Jet Model Fit

A two-component jet model can produce distinct behavior in the afterglow light curve. In the fit, there are 14 free parameters, and the narrow component and the wide component are denoted with the subscripts "n" and "w," respectively. The specific meanings of the parameters are shown in Appendix D. The best-fitting result and the posterior probability distributions of the parameters are presented in Table 3 and illustrated in Figures 10(a) and D1, respectively.

In this scenario, the early optical and X-ray afterglows are dominated by the narrow jet, while the late afterglows are dominated by the wide jet. As discussed in Section 3.4, it remains plausible for the wind environment. Therefore, we tested both the ISM and the wind case. The wind scenario provides a reasonable fit to the afterglow, with a BIC value of −1909. Meanwhile, the best-fitting result of the ISM scenario, as illustrated in Figure 10(a), yields a BIC value of −1918. It is strong evidence with $\Delta\mathrm{BIC} = 9$ that the smaller one offers a better fit to the data.

The narrow jet is strong, with $E_{0,\mathrm{n}} \approx 2.4 \times 10^{53}$ erg and $\Gamma_{0,\mathrm{n}} \approx 1259$. Typically, a normal GRB is expected. However, our line of sight deviates slightly from the narrow jet beam,[71] and the prompt emission will be significantly suppressed due to the strong Doppler beaming. To test this point, we consider an off-axis observer at ψ relative to the edge of the jet; the observed flux density could be expressed as (J. Granot et al. 2002; R. Yamazaki et al. 2003; W.-H. Lei et al. 2016; K. Ioka & T. Nakamura 2018; G. P. Lamb & S. Kobayashi 2019; P. Beniamini et al. 2023)

$$F_\nu(\psi, t) \sim F_{\nu/a_{\rm off}}(0, a_{\rm off} t) \begin{cases} a_{\rm off}^2 & ; \theta_{\rm j} < \theta_{\rm obs} \leqslant 2\theta_{\rm j}\,, \\ (\Gamma\theta_{\rm j})^2 a_{\rm off}^3 & ; \theta_{\rm obs} > 2\theta_{\rm j}\,, \\ a_{\rm off}^3 & ; \theta_{\rm j} \leqslant \Gamma^{-1}\,, \end{cases} \quad (2)$$

where $a_{\rm off} = \mathcal{D}_{\rm off}/\mathcal{D}_{\rm on} = (1-\beta_{\rm j})/(1-\beta_{\rm j}\cos\psi)$ is the ratio of the on-beam to the off-beam Doppler factor.

With the viewing angle $\theta_{\rm obs} \approx 1.^\circ 5$, Lorentz factor $\Gamma_{0,\mathrm{n}} \approx 1259$, and opening angle $\theta_{\rm j,n} \approx 1.15^\circ$ of the narrow jet, we correct the gamma-ray energy $E_{\gamma,\rm iso}$ and $E_{\rm peak}$ to the on-axis situation by using (J. Granot et al. 2002, 2017; K. Ioka & T. Nakamura 2018) $E^{\rm off}_{\gamma,\rm iso}/E^{\rm on}_{\gamma,\rm iso} \approx a^2_{\rm off}$ and $E^{\rm off}_{\rm peak}/E^{\rm on}_{\rm peak} \approx a_{\rm off}$. One can derive the on-axis gamma-ray energy $E^{\rm on}_{\gamma,\rm iso} \sim 2.0 \times 10^{55}$ erg and the on-axis observed peak energy $E^{\rm on}_{\rm peak} \sim 895$ keV, and the peak energy in the rest frame is 2393 keV with $z = 1.6734$. Note that for "BOAT" GRB 221009A, the investigations also reveal a physical picture involving two jet components, i.e., a narrow pencil-beam jet and a broader jet wing (M. V. Barkov & A. S. Pozanenko 2011; B. O'Connor et al. 2023; L. Rhodes et al. 2024; B. Zhang et al. 2024). The above on-axis $E^{\rm on}_{\gamma,\rm iso}$ and $E^{\rm on}_{\rm peak}$ of EP240801a are comparable to those of GRB 221009A ($(1.5 \pm 0.2) \times 10^{55}$ erg and 1435 ± 105 keV in the rest frame; Z.-H. An et al. 2023). Therefore, EP240801a could be similar to GRB 221009A but viewed slightly off-axis. We are observing the off-axis narrow beam emission, making EP240801a an XRF, if the prompt emission is mainly produced by the narrow jet.

Besides the narrow beam emission, the wide component contains small values of the kinetic energy ($E_{0,\rm w} \approx 8.5 \times 10^{52}$ erg) and the initial Lorentz factor ($\Gamma_{0,\rm w} \approx 45$). It is also possible that the bright core is missed by the observer, and the prompt emission of EP240801a is mainly produced by the weak wide jet.

4.2. Forward-reverse Shock Model Fit

In a thin shell FS-RS model, a "rebrightening" feature (a distinct RS peak and an FS peak) is expected in the optical light curve (B. Zhang et al. 2003). We therefore also consider this model to fit the afterglow of EP240801a.

[70] https://github.com/leiwh/PyFRS/

[71] The beam angle is given by $\max(\theta_{\rm j}, 1/\Gamma)$. The narrow beam jet is viewed off-axis if the observing angle $\theta_{\rm obs} > \max(\theta_{\rm j,n}, 1/\Gamma_{0,\rm n})$.

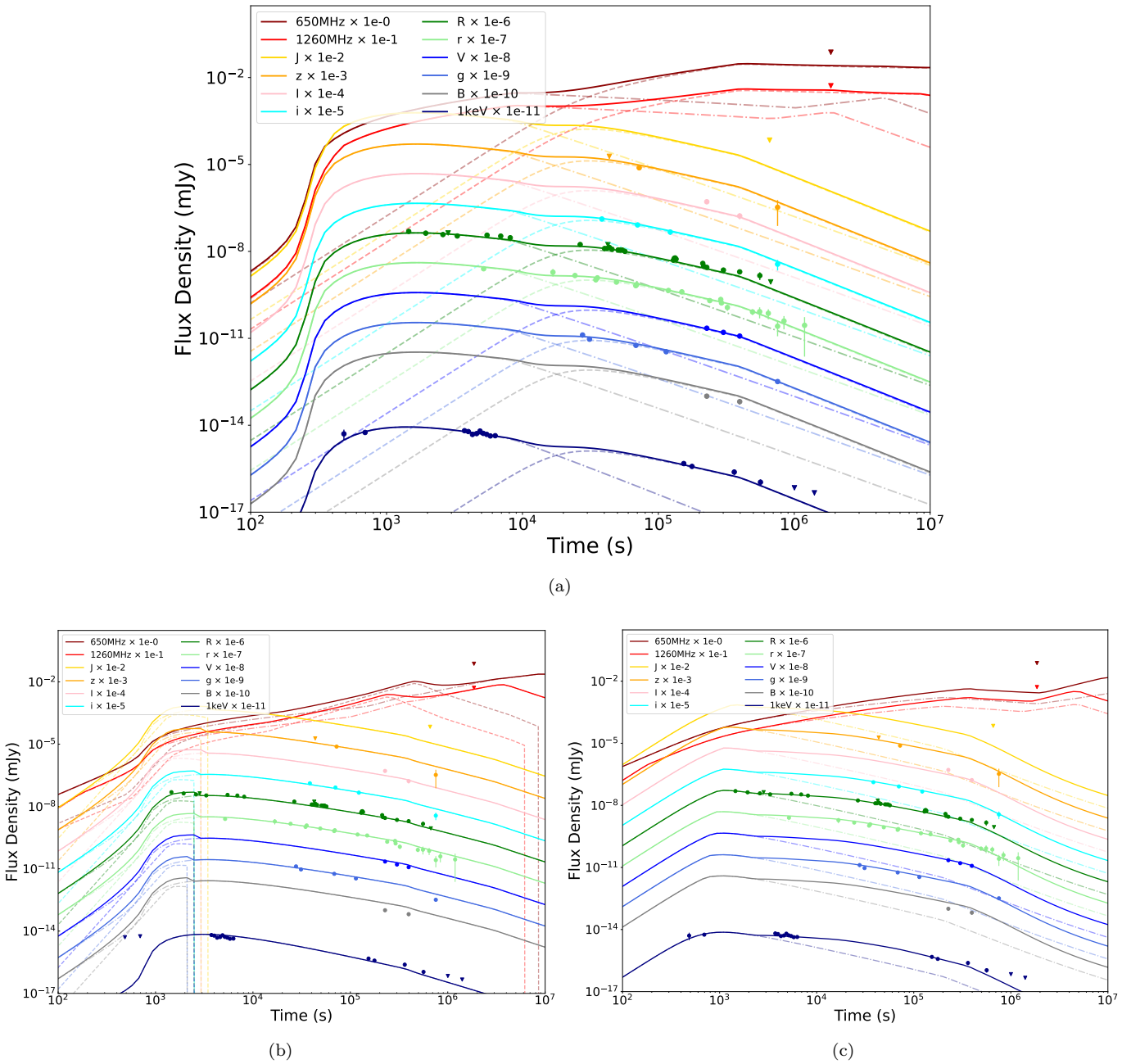

Figure 10. Best-fit results using the `PyFRS` code with three models (solid lines). (a) A two-component jet model, containing a narrow, faster jet (dashed–dotted lines) as well as a broad, slower jet (dashed lines). (b) FS-RS model. The contributions from the RS and FS are plotted with dashed lines and dashed–dotted lines, respectively. (c) FS with energy injection (solid lines). The FS without energy injection is represented by the dashed–dotted lines.

There are 11 free parameters, and the FS and RS components are denoted with the subscripts "f" and "r," respectively. The two EP/FXT data points at the end of the steep decline cannot be reproduced with this model; we just set them as upper limits in the afterglow fit in this case. The best-fitting results are presented in Table 3 and illustrated in Figure 10(b).

The FS-RS model fit result also implies that EP240801a is observed off-axis ($\theta_{\rm obs} \approx 10.^{\circ}5$ versus $\theta_{\rm j} \approx 9^{\circ}$). In the same way as done in Section 4.1, we correct the gamma-ray energy $E_{\gamma,\rm iso}$ and also $E_{\rm peak}$ to the on-axis situation. One can derive the on-axis gamma-ray energy $E^{\rm on}_{\gamma,\rm iso} \sim 4.3 \times 10^{54}$ erg and the on-axis observed peak energy $E^{\rm on}_{\rm peak} \sim 412$ keV, appeared as a bright type II GRB.

A magnetically dominated jet does not provide an RS (B. Zhang & S. Kobayashi 2005). If the early phase of the *R*-band light curve is shaped by the FS-RS emission, then the RS should not be strongly magnetized. Based on the fit with the FS-RS model, we infer that the magnetic field strength ratio in the RS and FS is $R_{\rm B} \equiv B_{\rm r}/B_{\rm f} \approx 3.5$. Such a mild $R_{\rm B}$ is consistent with the forward-reverse shock interpretation.

4.3. Energy Injection Model Fit

The X-ray and optical shallow decay can also be interpreted in the FS model with energy injection due to late-time central engine activity. The best-fitting results are presented in Table 3 and illustrated in Figure 10(c).

Table 3
Parameters of Afterglow Modeling

Parameter	Unit	Prior Type	Prior	Results				
				Two-component Jet		FS+RS		Energy Injection
				Narrow	Wide	FS	RS	
n_{18}	cm^{-3}	Log-uniform	$[10^{-5}, 10^{3}]$	$(2.24^{+6.27}_{-1.70}) \times 10^{-3}$		$5.37^{+15.05}_{-3.82}$		$8.13^{+5.05}_{-4.24}$
θ_{obs}	deg	Uniform	[0.01, 45]	$1.50^{+0.45}_{-0.35}$		$10.51^{+2.01}_{-1.51}$		$8.01^{+5.15}_{-5.08}$
E_0	erg	Log-uniform	$[10^{51}, 10^{56}]$	$(2.40^{+10.48}_{-1.89}) \times 10^{53}$	$(8.51^{+23.11}_{-5.20}) \times 10^{52}$	$(1.58^{+0.28}_{-0.44}) \times 10^{53}$		$(5.01^{+2.40}_{-1.12}) \times 10^{51}$
Γ_0	1	Log-uniform	[1, 2000]	$1258.93^{+439.32}_{-427.16}$	$44.67^{+14.22}_{-10.00}$	$199.53^{+40.36}_{-41.04}$		$40.74^{+6.04}_{-3.58}$
θ_j	deg	Uniform	[0.01, 45]	$1.15^{+0.35}_{-0.27}$	$5.25^{+1.49}_{-1.31}$	$9.03^{+1.73}_{-1.30}$		$15.73^{+1.30}_{-1.62}$
p	1	Uniform	[2.01, 4.0]	$2.28^{+0.01}_{-0.01}$	$2.43^{+0.02}_{-0.02}$	$2.05^{+0.02}_{-0.02}$	$2.47^{+0.37}_{-0.20}$	$2.35^{+0.02}_{-0.02}$
ϵ_e	1	Log-uniform	$[10^{-4}, 0.5]$	$(6.31^{+10.29}_{-4.72}) \times 10^{-2}$	$(3.72^{+0.86}_{-0.96}) \times 10^{-1}$	$(4.37^{+1.80}_{-0.90}) \times 10^{-2}$	$(3.39^{+0.50}_{-0.82}) \times 10^{-1}$	$(3.89^{+0.68}_{-1.01}) \times 10^{-1}$
ϵ_B	1	Log-uniform	$[10^{-4}, 0.5]$	$(2.57^{+25.61}_{-2.47}) \times 10^{-3}$	$(1.91^{+8.09}_{-1.66}) \times 10^{-3}$	$(7.41^{+9.18}_{-4.25}) \times 10^{-4}$	$(9.33^{+135.21}_{-8.42}) \times 10^{-3}$	$(1.38^{+0.66}_{-0.28}) \times 10^{-4}$
L_0	$erg\ s^{-1}$	Log-uniform	$[10^{45}, 10^{54}]$	...	...	...	...	$(1.38^{+0.81}_{-0.47}) \times 10^{48}$
t_0	s	Log-uniform	$[10^{3}, 10^{4}]$	...	...	...	...	$977.24^{+144.78}_{-218.66}$
t_e	s	Log-uniform	$[10^{3}, 10^{7}]$	...	...	...	...	$4897.79^{+1709.15}_{-1095.89}$
q	1	Uniform	[–2, 2]	...	...	...	...	$0.11^{+0.27}_{-0.35}$

We consider two popular models for the energy injection: spin-down of a magnetar and fallback accretion onto a stellar mass black hole. The characteristic spin-down luminosity L_0 of a magnetar is (B. Zhang & P. Mészáros 2001)

$$L_0 = 1.0 \times 10^{49} \, (B_{p,15}^2 P_{0,-3}^{-4} R_6^6) \, \mathrm{erg \, s^{-1}}, \quad (3)$$

where $B_{\mathrm{p},15} = B_{\mathrm{p}}/(10^{15}\,\mathrm{G})$, $P_{0,-3} = P_0/(10^{-3}\,\mathrm{ms})$, and $R_6 = R/(10^6\,\mathrm{cm})$. B_{p}, P_0, and R are the magnetic field, spin period, and radius of the magnetar.

For the black hole central engine model, late energy injection is dominated by the Blandford–Znajek (BZ) mechanism (T. Liu et al. 2015; W.-H. Lei et al. 2017). The BZ power can be rewritten as a function of mass accretion rate as (W.-H. Lei et al. 2013)

$$L_{\mathrm{BZ}} = 9.3 \times 10^{48} \frac{a_\bullet^2 \dot{m}_{-5} F(a_\bullet)}{(1 + \sqrt{1 - a_\bullet^2})^2} \quad \mathrm{erg \, s^{-1}}, \quad (4)$$

where $\dot{m}_{-5} = \dot{M}/(10^{-5} M_\odot \ \ \mathrm{s^{-1}})$ is the dimensionless accretion rate, $a_\bullet = J_\bullet c/(G M_\bullet^2)$ is the spin parameter of the black hole, $F(a_\bullet) = [(1 + q_a^2)/q^2][(q_a + 1/q_a)\arctan q_a - 1]$, and $q_a = a_\bullet/(1 + \sqrt{1 - a_\bullet^2})$.

As we can see, both central engine models can give rise to the energy injection required for typical values of the parameters of the objects involved. The values of the jet parameters are quite close to those of the wide jet of the two-component jet model, i.e., kinetic energy $E_0 \sim 10^{52}$ erg and Lorentz factor $\Gamma_0 < 50$, making it possible to produce an XRF like EP240801a.

5. Summary

In this Letter, we present comprehensive multiband observations with the facilities mentioned in Appendix A of EP240801a, an extremely soft GRB detected by EP. The physical origin of such a burst is still unclear. Our rich data set, especially the early X-ray and optical observations of EP240801a, enable us to explore its nature.

Our conclusions are summarized as follows.

(1) We identified the redshift of EP240801a as $z = 1.6734 \pm 0.0002$ through the significant Mg II doublet and Fe II absorption lines that appear in the GTC and Keck spectra, assuming the transient occurred in the host galaxy at that redshift.

(2) We performed a joint fit for the prompt emission phase with EP/WXT and Fermi/GBM data, deriving $E_{\gamma,\mathrm{iso}} = 5.57^{+0.54}_{-0.50} \times 10^{51}$ erg, $E_{\mathrm{peak}} = 14.90^{+7.08}_{-4.71}$ keV, and the fluence ratio $S(25\text{–}50\ \mathrm{keV})/S(50\text{–}100\ \mathrm{keV}) = 1.67^{+0.74}_{-0.46}$ for EP240801a. These values suggest that EP240801a is an XRF.

(3) We fit the available host-galaxy photometry with `Prospector` and use the best-fit model photometry to subtract the contribution of the host galaxy from the observed data.

(4) The R-band light curve shows a shallow phase followed by a normal decay phase, suggesting that multiple components are involved. Three models—a two-component jet model, an FS-RS model, and a jet model with energy injection—are employed to elucidate the multiband afterglow data.

(i) The fit with the two-component jet model suggests an off-axis narrow jet and a weak wide jet. We find that EP240801a would be similar to the "BOAT" GRB 221009A if corrected to an on-axis view. Therefore, the XRF EP240801a can be interpreted as the off-axis narrow beam emission or the wide jet emission.

(ii) The FS-RS modeling also suggests an off-axis jet. The fit results for kinetic energy ($E_0 \sim 1.6 \times 10^{53}$ erg) and initial Lorentz factor ($\Gamma \sim 200$) are consistent with a typical GRB. The modeling indicates that the RS/FS magnetic field strength ratio is $R_{\mathrm{B}} \equiv B_{\mathrm{r}}/B_{\mathrm{f}} \approx 3.5$. Such a mild R_{B} is also consistent with the forward-reverse shock interpretation.

(iii) The energy injection model fit also involves a weak jet as the wide jet in the two-component jet model. Both the magnetar and the black hole central engine models can explain the energy injection required for typical values of the parameters. Therefore, EP240801a can also be interpreted as an intrinsically weak GRB.

With early multiband observations, i.e., those conducted earlier than 1 ks, we can obtain more information that helps us to distinguish whether the event is due to an off-axis scenario, an RS, or an intrinsically weak GRB.

Future EP detections might discover a number of XRFs like EP240801a, which in turn would help to comprehend the physics behind such events. Especially, the very early X-ray and optical follow-ups would be crucial to distinguish between the three origin models for EP240801a-like events, i.e., from a two-component jet similar to GRB 221009A whose bright narrow core is missed by the observer, an off-axis normal GRB, or a faint GRB (e.g., due to inefficient jet breakout from the progenitor star). These studies could be helpful in answering the question of whether narrow beam GRBs like 221009A are common.

Acknowledgments

The data presented herein were obtained in part with ALFOSC, which is provided by the Instituto de Astrofisica de Andalucia (IAA) under a joint agreement with the University of Copenhagen and NOT. The optical spectrum was obtained at the W. M. Keck Observatory, which is operated as a scientific partnership among the California Institute of Technology, the University of California, and NASA; the observatory was made possible by the generous financial support of the W. M. Keck Foundation. KAIT and its ongoing operation were made possible by donations from Sun Microsystems, Inc., the Hewlett-Packard Company, AutoScope Corporation, Lick Observatory, the U.S. NSF, the University of California, the Sylvia & Jim Katzman Foundation, and the TABASGO Foundation. Research at Lick Observatory is partially supported by a generous gift from Google.

D.X. acknowledges the science research grants from the China Manned Space Project with Nos. CMS-CSST-2021-A13 and CMS-CSST-2021-B11. This work is supported by the National Natural Science Foundation of China under grant 12473012. A.V.F.'s research group at UC Berkeley acknowledges financial assistance from the Christopher R. Redlich Fund, Gary and Cynthia Bengier, Clark and Sharon Winslow, Alan Eustace (W.Z. is a Bengier–Winslow–Eustace Specialist in Astronomy), William Draper, Timothy and Melissa Draper, Briggs and Kathleen Wood, Sanford Robertson (T.G.B. is a

Draper–Wood–Robertson Specialist in Astronomy), and numerous other donors. T.-W.C. and A.A. acknowledge the Yushan Young Fellow Program by the Ministry of Education, Taiwan, for the financial support (MOE-111-YSFMS-0008-001-P1). S.Y. acknowledges the funding from the National Natural Science Foundation of China under grant No. 12303046 and the Henan Province High-Level Talent International Training Program. O.A.B. and A.S.P. thank the Ministry of Higher Education, Science and Innovation of the Republic of Uzbekistan for financial support, project No. IL-5421101855. N.S.P. thanks the Russian Science Foundation (project 23-12-00198) for support in processing optical observation data of gamma-ray burst afterglow. V.K. and M.K. acknowledge the Ministry of Science and Higher Education of the Republic of Kazakhstan (project No. BR 24992807 "Development of Kazakhstan digital environment for astronomical research of near and deep space objects within the international virtual observatory network") for the observations carried out using the AZT-20 telescope. F.E.B. acknowledges support from ANID-Chile grants: BASAL CATA FB210003, FONDECYT Regular 1241005, and Millennium Science Initiative, AIM23-0001. J.Q.V. acknowledges support from the European Union's Horizon 2020 research and innovation program grant agreement No. 101095973 and the IAU-Gruber foundation fellowship. M.E.R. acknowledges support from the European Union's Horizon 2020 research and innovation program grant agreement No. 101095973. A.J.C.T. acknowledges support from the Spanish Ministry projects PID2020-118491GB-I00 and PID2023-151905OB-I00 and Junta de Andalucía grant P20_010168. M.A.P.T. and D.M.S. acknowledge support by the Spanish Ministry of Science via the Plan de Generacion de conocimiento PID2021-124879NB-I00. D.M.S. also acknowledges support via a Ramon y Cajal Fellowship RYC2023-044941. J.M. acknowledges the financial support of the National Key R&D Program of China (2023YFE0101200), Natural Science Foundation of China 12393813, and the Yunnan Revitalization Talent Support Program (YunLing Scholar Project).

Facilities: EP (WXT and FXT), Fermi (GBM), Keck:I (LRIS), KAIT, BOOTES, LCOGT, CrAO:Shajn, NOT (ALFOSC), BAT, GTC (OSIRIS+, HiPERCAM, and EMIR), VLT:Yepun (HAWK).

Appendix A
The Photometric Results

The information of all telescopes in Table A1 is as follows: the 0.76 m Katzman Automatic Imaging Telescope (KAIT; located at Lick Observatory, California, United States); the 0.6 m robotic telescope of the Burst Observer and Optical Transient Exploring System (BOOTES-7; located at San Pedro de Atacama, Chile); the 1 m telescope at the Las Cumbres Observatory (LCO; located at Siding Springs Observatory, New South Wales, Australia); the 0.7 m telescope of the TRT network (located at Sierra Remote Observatories, California, United States); the 0.40 m SLT (located at Lulin Observatory, Taiwan); the 2.4 m Gao-Mei-Gu telescope (GMG; located at the Lijiang Observatory, Yunnan, China); the 1.0 m JinShan 100C telescope (ALT/100C; located at Altay Observatory, Xinjiang, China); the 1.5 m AZT-22 telescope of Maidanak Astrophysical Observatory (located at Qashqadaryo Viloyati, Uzbekistan); the 2.6 m ZTSh

Table A1
The Photometric Results of Our Observations Combined with Collected GCN Results

ΔT (days)	Band	Magnitude[a] (AB)	Telescope Inst.	Reference
0.0169	Clear	19.89 ± 0.07	KAIT	This work
0.0225	Clear	20.04 ± 0.06	KAIT	This work
0.0301	Clear	20.16 ± 0.06	KAIT	This work
0.0331	Clear	> 19.80	BOOTES-7	This work
0.0384	Clear	20.28 ± 0.09	KAIT	This work
0.0600	*r*	20.61 ± 0.08	LCO	This work
0.0635	Clear	20.21 ± 0.08	KAIT	This work
0.0801	Clear	20.29 ± 0.09	KAIT	This work
0.0941	*R*	20.43 ± 0.17	TRT	This work
0.1940	*r*	20.90 ± 0.30	SLT	GCN 37002 (A. Aryan et al. 2024)
0.2818	*r*	21.17 ± 0.11	SLT	This work
0.3077	*R*	21.00 ± 0.12	GMG	This work
0.3204	*g*	21.43 ± 0.20	LCO	GCN 37007 (I. Pérez--Fournon et al. 2024)
0.3604	*g*	21.78 ± 0.07	ALT/100C	This work
0.4012	*r*	21.52 ± 0.07	ALT/100C	This work
0.4120	*r*	21.36 ± 0.15	SLT	This work
0.4445	*i*	21.25 ± 0.09	ALT/100C	This work
0.4649	*R*	21.33 ± 0.04	AZT-22	This work
0.4839	*R*	21.33 ± 0.03	ZTSh	This work
0.4928	*R*	>21.00	AS-32	This work
0.5044	*z*	>20.70	ALT/100C	This work
0.5058	*R*	21.25 ± 0.02	ZTSh	This work
0.5276	*R*	21.39 ± 0.02	ZTSh	This work
0.5687	*r*	21.70 ± 0.03	NOT	This work
0.5852	*R*	21.45 ± 0.02	ZTSh	This work
0.6071	*R*	21.46 ± 0.02	ZTSh	This work
0.6289	*R*	21.46 ± 0.02	ZTSh	This work
0.6383	*R*	21.50 ± 0.10	Z-1000	This work
0.6563	*R*	21.56 ± 0.02	ZTSh	This work
0.7898	*r*	21.98 ± 0.05	GTC	This work
0.7911	*g*	22.28 ± 0.04	NOT	This work
0.8019	*r*	21.89 ± 0.04	NOT	This work
0.8135	*i*	21.73 ± 0.04	NOT	This work
0.8363	*z*	21.69 ± 0.09	NOT	This work
1.3209	*g*	22.78 ± 0.13	ALT/100C	This work
1.3730	*r*	22.34 ± 0.10	ALT/100C	This work
1.4155	*i*	22.28 ± 0.18	ALT/100C	This work
1.4935	*R*	22.26 ± 0.08	ZTSh	This work
1.5038	*R*	22.20 ± 0.15	Z-1000	This work
1.5155	*R*	22.12 ± 0.07	ZTSh	This work
1.5374	*R*	22.09 ± 0.07	ZTSh	This work
1.5620	*R*	22.18 ± 0.08	ZTSh	This work
1.7225	*r*	22.44 ± 0.04	NOT	This work
2.4565	*R*	22.51 ± 0.12	ZTSh	This work
2.4937	*R*	22.72 ± 0.1	AZT-22	This work
2.6284	*B*	23.90 ± 0.08	BTA	This work
2.6287	*I*	22.15 ± 0.07	BTA	This work
2.6287	*R*	22.80 ± 0.05	BTA	This work
2.6290	*V*	23.08 ± 0.06	BTA	This work
2.7656	*r*	23.03 ± 0.07	NOT	This work
3.3305	*r*	22.96 ± 0.16	ALT/100C	This work
3.3733	*r*	23.17 ± 0.11	AZT-20	This work
3.4843	*V*	23.36 ± 0.07	BTA	This work
3.4852	*R*	22.99 ± 0.04	BTA	This work
3.7278	*r*	23.42 ± 0.13	NOT	This work
4.5923	*R*	23.11 ± 0.05	BTA	This work
4.5924	*I*	23.09 ± 0.15	BTA	This work
4.5925	*B*	24.21 ± 0.10	BTA	This work
4.5925	*V*	23.59 ± 0.10	BTA	This work
5.7072	*r*	23.63 ± 0.08	NOT	This work
6.4371	*r*	23.62 ± 0.21	AZT-20	This work

Table A1
(Continued)

ΔT (days)	Band	Magnitude[a] (AB)	Telescope Inst.	Reference
6.4555	*R*	23.35 ± 0.22	AZT-22	This work
7.4579	*r*	23.69 ± 0.17	AZT-20	This work
7.6233	*J*	>21.80	SAI-25	This work
7.7625	*R*	>24.03	AZT-22	This work
8.7252	*u*	25.48 ± 0.09	GTC	This work
8.7252	*g*	24.54 ± 0.03	GTC	This work
8.7252	*r*	24.09 ± 0.04	GTC	This work
8.7252	*i*	24.01 ± 0.06	GTC	This work
8.7252	*z*	23.72 ± 0.09	GTC	This work
8.7595	*H*	21.52 ± 0.20	GTC	This work
9.7213	*r*	23.96 ± 0.12	NOT	This work
13.7801	*r*	24.07 ± 0.22	NOT	This work
21.5166	650 MHz	>75	GMRT	GCN 37468 (A. Balasubramanian et al. 2024)
21.5166	1260 MHz	>52	GMRT	GCN 37468 (A. Balasubramanian et al. 2024)
26.8144[b]	*g*	25.13 ± 0.11	GTC	This work
26.8144[b]	*r*	24.42 ± 0.09	GTC	This work
26.8144[b]	*i*	24.53 ± 0.16	GTC	This work
26.8144[b]	*z*	25.13 ± 0.28	GTC	This work
26.8148	*u*	>24.03	GTC	This work
30.6745[b]	*r*	24.40 ± 0.19	NOT	This work
37.6434[b]	*i*	24.46 ± 0.20	NOT	This work
53.7992	*Ks*	>21.10	GTC	This work
59.7570[b]	*Ks*	22.12 ± 0.29	VLT	This work

Notes. ΔT is the exposure median time after T_0. Magnitudes in the AB system (J. B. Oke & J. E. Gunn 1983) are not corrected for Galactic extinction, which is $E(B-V) = 0.093$ (E. F. Schlafly & D. P. Finkbeiner 2011).
[a] We calibrated the magnitudes of the KAIT Clear band with the *R*-band reference star magnitudes, as its effective wavelength is roughly *R*. For radio observations, the flux density unit is μJy. The errors are statistical only.
[b] For these observations, they are mostly attributed to the host-galaxy flux; therefore, we take them as host-galaxy magnitudes.

telescope of the Crimean Astrophysical Observatory (located in Crimea); the 0.7 m AS-32 telescope of the Abastumani Observatory (located at Abastumani-Kanobili, Georgia); the 2.56 m NOT (located at the Roque de los Muchachos Observatory, La Palma, Spain); the 1 m ZEISS-1000 telescope (Z-1000; located at the Special Astrophysical Observatory, Karachay-Cherkessia, Russia); the 10.4 m GTC (Roque de los Muchacos Observatory, La Palma, Spain); the 10 m Keck I telescope (located at Maunakea, Hawaii, United States); the 6 m BTA telescope (located at the Special Astrophysical Observatory, Karachay-Cherkessia, Russia); the 1.5 m AZT-20 telescope of Assy-Turgen Observatory (located at Almaty, Kazakhstan); the 2.5 m SAI-25 alt-azimuth reflector at the Caucasian Mountain Observatory of the Sternberg Astronomical Institute (located at Karachay-Cherkessia, Russia), and the 8.2 m VLT (located at Paranal Observatory, Antofagasta Region, Chile).

Appendix B
Optical Photometry and Spectroscopy

After standard data reduction with `IRAF` (D. Tody 1986), the HiPERCAM pipeline, and the pyEMIR pipeline and astrometric calibration by Astrometry.net (D. Lang et al. 2010), the optical photometry was calibrated with the Legacy Surveys Data Release 10 (A. Dey et al. 2019) and the Sloan Digital Sky Survey Data Release 18 (A. Almeida et al. 2023), while the NIR data were calibrated with the Two Micron All Sky Survey catalog (M. F. Skrutskie et al. 2006). The photometry in the Johnson–Cousin filters were calibrated with the converted magnitude from the Sloan system[72] for the nearby reference stars. It should be noted that there may be an additional systematic error for the differential photometry of the u', *H*, *Ks* bands, as the catalogs are significantly shallower than the target.

The OSIRIS+ observations utilized the 1″ wide slit oriented along the parallactic angle and the R1000R grism, which has a coverage of 5100–10000 Å. The data reduction followed bias subtraction and flat-field correction using the standard `PyRAF` tasks (Science Software Branch at STScI 2012) and cosmic-ray correction with the `LACosmic` task (P. G. van Dokkum 2001).

For Keck/LRIS, the spectrum was acquired with the slit oriented near the parallactic angle to minimize slit losses caused by atmospheric dispersion (A. V. Filippenko 1982). The LRIS observations utilized the 1″ wide slit, 600/4000 grism, and 400/8500 grating, which produced a spectral coverage of 3140–10270 Å. Data reduction followed standard techniques for CCD processing and spectrum extraction using the LPipe data reduction pipeline (D. A. Perley 2019). Low-order polynomial fits to comparison-lamp spectra were used to calibrate the wavelength scale, and small adjustments derived from night-sky lines in the target frames were applied. The spectrum was flux calibrated using observations of appropriate spectrophotometric standard stars observed on the same night, at similar air masses, and with an identical instrument configuration; these standard-star spectra were also used to remove telluric absorption.

Appendix C
Host Galaxy

For the chance alignment probability, we determined the number density of sources brighter than or as bright as the galaxy in a region of 60″ × 60″ centered around EP240801a. Then, assuming Poisson statistics, we calculated that the chance alignment for this galaxy is $P_{\rm chance} = 0.002$.

`Prospector` is software for SED fitting to constrain the host-galaxy properties. The *parametric sfh* template in `Flexible Stellar Population Synthesis` (C. Conroy et al. 2009; C. Conroy & J. E. Gunn 2010) was used, and the redshift is fixed to 1.6734. The extinction of the host galaxy is assumed to be consistent with the Milky Way extinction law. The model photometry results in the u', z', *B*, *V*, *R*, *I*, *H* bands were adopted to correct the contribution of the host galaxy for the optical data of EP240801a in those bands, and we adopted the rms error as their error.

Appendix D
Afterglow Model and the Fitting

The closure relation analysis for EP240801a prefers an ISM environment (a constant external medium). We thus consider a relativistic shell with energy E_0, initial bulk Lorentz factor Γ_0, and opening angle θ_j advancing in an ISM. A pair of shocks

[72] https://www.sdss4.org/dr12/algorithms/sdssUBVRITransform/

will be produced (M. J. Rees & P. Meszaros 1992; P. Mészáros & M. J. Rees 1997; R. Sari et al. 1998; S. Kobayashi et al. 1999; R. Sari & T. Piran 1999; Y. C. Zou et al. 2005; G. P. Lamb et al. 2019): an FS (propagating into the external medium) and an RS (propagating into the shell). There are four regions separated by the two shocks: region 1, the ISM with density n_1; region 2, the shocked medium; region 3, the shocked shell material; and region 4, the unshocked shell material with density n_4.

For the FS, the dynamics are described with four phases: the coasting phase (the Lorentz factor is nearly constant, $\Gamma \approx \Gamma_0$), the deceleration phase (the shell starts to decelerate when the mass of the medium swept by the FS is about $1/\Gamma_0$ of the rest mass in the ejecta), the post-jet-break phase (when the $1/\Gamma$ cone becomes larger than θ_j), and the Newtonian phase (when the rest-mass energy of the swept-up medium becomes comparable to the energy of the ejecta). The overall evolution of the shell, covering the above four phases, is determined by (Y. F. Huang et al. 2000)[73]

$$\frac{dR}{dt} = \beta_j c\Gamma(\Gamma + \sqrt{\Gamma^2 - 1}), \tag{D1}$$

$$\frac{dm}{dR} = 2\pi R^2(1 - \cos\theta_j) n_1 m_p, \tag{D2}$$

$$\frac{d\Gamma}{dm} = -\frac{\Gamma^2 - 1}{M_{ej} + 2\Gamma m}, \tag{D3}$$

where R is the radius of the event in the burst frame, t is the observer time, m is the swept-up mass, $M_{ej} = E_0(1 - \cos\theta_j)/2(\Gamma_0 - 1)c^2$ is the ejecta mass, m_p is the proton mass, and $\beta_j = \sqrt{1 - \Gamma^{-2}}$.

If there is energy injection from the GRB central engine, Equation (D3) should be replaced by (J. J. Geng et al. 2013)

$$\frac{d\Gamma}{dm} = -\frac{\Gamma^2 - 1 - \frac{1-\beta_j}{\beta_j c^3} L_{inj} dR/dm}{M_{ej} + 2\Gamma m}. \tag{D4}$$

During the injection time, $t_{start} < t < t_{end}$, the injected luminosity is $L_{inj} = L^0_{inj}(t/t_{start})^{-q}$, where L^0_{inj} is the initial injection power, q is the decay power-law index, and t_{start} and t_{end} are, respectively, the start and end time for energy injection.

We assume that a constant fraction ϵ_e of the FS energy $e_2 = 4\Gamma^2 n_1 m_p c^2$ is deposited into electrons, accelerating them to a power-law distribution $N(\gamma_e) \propto \gamma_e^{-p}$. This defines the minimum injected electron Lorentz factor, $\gamma_m = \frac{p-2}{p-1}\epsilon_e(\Gamma - 1)\frac{m_p}{m_e}$, where m_e is the electron mass. A fraction ϵ_B of the shock energy resides in the magnetic field with $B = (32\pi m_p \epsilon_B n_0)^{1/2} c$. The critical electron Lorentz factor $\gamma_c = (6\pi m_e c)/(\Gamma\sigma_T B^2 t)$ is given by setting the electron's lifetime equal to the time t, and electrons with $\gamma_e > \gamma_c$ will be significantly cooled due to synchrotron radiation.

Combining the radiative cooling and the continuous injection of new accelerated electrons, coupled with the synchrotron self-absorption effect, leads to a broken power-law spectrum. This spectrum is segmented into several sections based on three characteristic frequencies (R. Sari et al. 1998; R. A. Chevalier & Z.-Y. Li 2000; J. Granot & R. Sari 2002; S. Kobayashi & B. Zhang 2003; X. F. Wu et al. 2003; Y. C. Zou et al. 2005; H. J. Van Eerten & R. A. M. J. Wijers 2009; H. Gao et al. 2013; B. Zhang 2018): ν_m (defined by γ_m), ν_c (defined by γ_c), and ν_a (characterized by synchrotron self-absorption).

Considering the contribution of the RS, a "rebrightening" feature (a distinct RS peak and an FS peak) is expected in the optical light curve (B. Zhang et al. 2003) for a thin shell interacting with a constant-density ISM. Therefore, the optical afterglow behavior (R band) of EP240801a can also be explained with the thin-shell forward-reverse shock (FS-RS) model.

In the thin-shell case, the RS is Newtonian during the shock-crossing phase (S. Kobayashi 2000; B. Zhang et al. 2003). The scalings before the RS crossing time t_{dec} are (S. Kobayashi 2000)

$$\gamma_3 \approx \Gamma_0, \quad n_3 \approx 7 n_1 \Gamma_0^2 (t/t_{dec})^{-3},$$
$$e_3 \approx 4\Gamma_0^2 n_1 m_p c^2, \quad N_{e,3} \approx N_0 (t/t_{dec})^{3/2}, \tag{D5}$$

where $N_0 = M_{ej}/m_p$ is the total number of electrons in the ejecta.

After the RS crosses the shell, the shell expands adiabatically in the shell's comoving frame, and the jet enters the deceleration phase. The dynamical behavior in region 3 is expressed with the scalings (S. Kobayashi 2000; H. Gao et al. 2013; B. Zhang 2018)

$$\gamma_3 \propto t^{-2/5}, \quad n_3 \propto t^{-6/7}, \quad e_3 \propto t^{-8/7}, \quad N_{e,3} = N_0. \tag{D6}$$

In the same way as in the FS, we also assume that electrons are accelerated at the RS front to a power-law distribution, and a fraction of the RS energy e_3 is distributed into electrons and a fraction to the magnetic field in region 3. The spectrum is also segmented into a broken power law by ν_m, ν_c, and ν_a.

In our MCMC fitting with `PyFRS`, we set the walkers as tenfold the number of free parameters (i.e., 140 for the two-component jet model, see its result in Figure D1) running 30,000 steps and discarded the first 15,000 steps as burn-in to explore the parameter space. The early steep decay phase at several 100 s, as observed by EP/FXT, is not included in the afterglow fit, as these data are likely dominated by the prompt emission. However, the two data points at the end of the steep decline deviate from the single power-law fit to these data ($\alpha \sim 5.82 \pm 0.32$) and are thus considered in the afterglow fit. The model photometric results of the host galaxy in the u' and H bands may have an additional systematic error, given that their wavelengths are located at the edges of the fitting data. Thus, the u'- and H-band data are excluded from the fit due to their potential systematic errors, whether arising from the differential photometry or from the host-galaxy model photometric results. In the MCMC fitting, we have common free parameters like the isotropic kinetic energies E_0, the initial Lorentz factors Γ_0, the jet opening angles θ_j, the viewing angle θ_{obs}, the number density of the ISM n_1 (n_{18} in the `PyFRS` code, defined as the density at $R = 10^{18}$ cm), the electron distribution

[73] Equation (D3) is an approximate description of the blast-wave dynamics. A rigorous treatment after correctly describing the internal energy, adiabatic loss, and total energy should be (L. Nava et al. 2013; B. Zhang 2018)

$$\frac{d\Gamma}{dR} = -\frac{(\Gamma_{eff} + 1)(\Gamma - 1)c^2 \frac{dm}{dR} + \Gamma_{eff}\frac{dU_{ad}}{dr}}{(M_{ej} + m)c^2 + U\frac{d\Gamma_{eff}}{d\Gamma}},$$

where $\Gamma_{eff} = (\hat{\gamma}\Gamma^2 - \hat{\gamma} + 1)/\Gamma$, U is the internal energy in the comoving frame, and dU_{ad} is the adiabatic loss. This equation can be reduced to Equation (D3) by adopting $\hat{\gamma} = 1$ (neglecting the pressure term), $dU_{ad}/dR = 0$ (neglecting adiabatic loss), $U = (\Gamma - 1)mc^2$, and $\Gamma_{eff} \simeq \hat{\gamma}\Gamma$ (for $\Gamma \gg 1$).

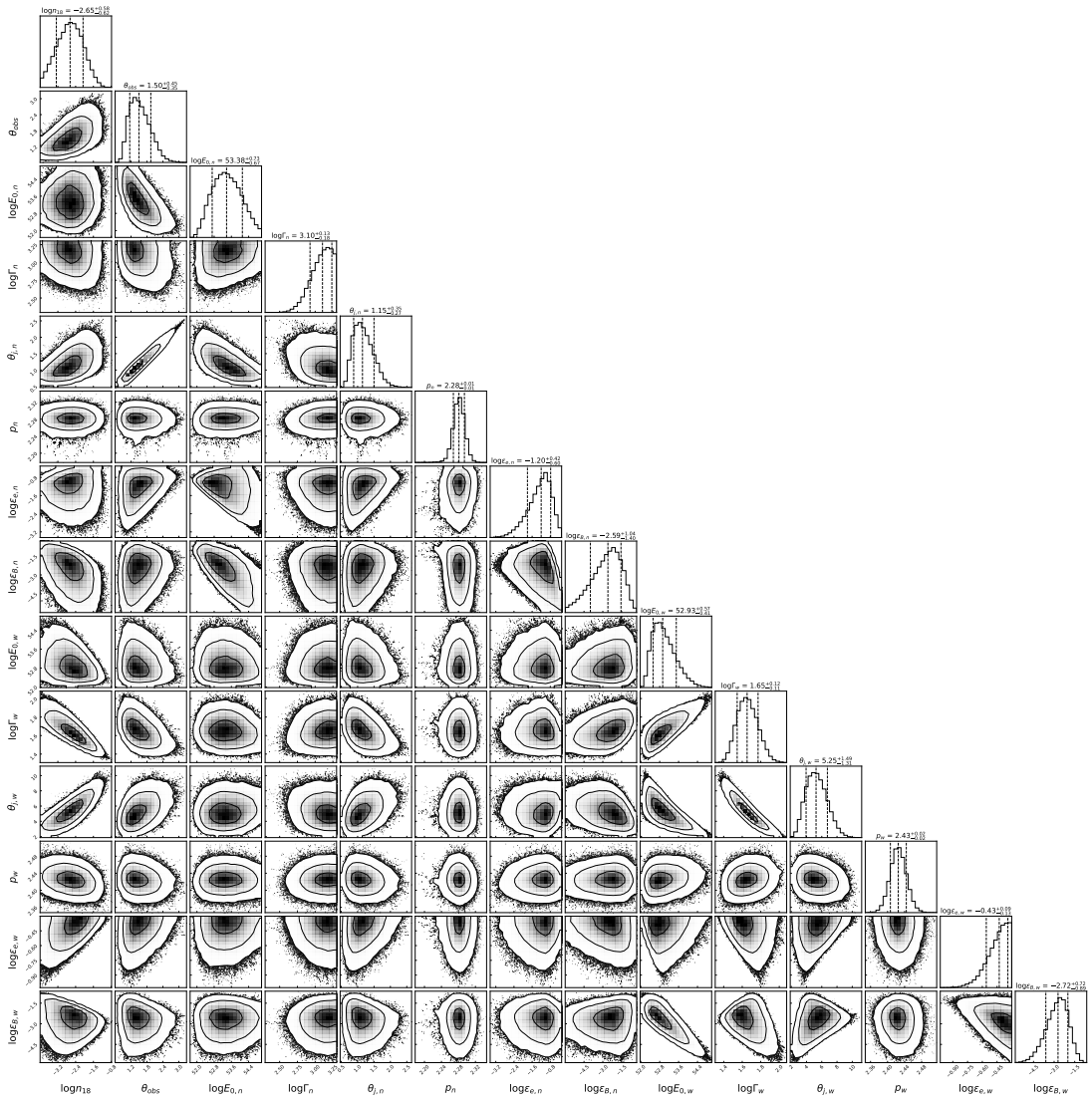

Figure D1. Posterior probability distributions of the afterglow parameters were obtained using the two-component jet modeling of EP240801a. The median values with the 1σ regions are shown in the 1D probability distribution.

power-law indices p, the energy fractions in electrons ϵ_e, and the energy fractions in the magnetic field ϵ_B. For the two-component jet model, there are two distinct components: a narrow component and a wide component. Each of these components has its own set of parameters, including E_0, Γ_0, θ_j, p, ϵ_e, and ϵ_B. In contrast to the FS, the RS has its own values of p, ϵ_e, and ϵ_B. For the energy injection model, we have four more parameters: the luminosity L_0, power-law index q, start time t_0, and end time t_e.

We tested the wind scenario as well; the wind model fails to explain the behavior of the optical and X-ray data between 1 and 10 ks using the forward-reverse shock model and energy injection model. It provides a reasonable fit with the structured jet model.

ORCID iDs

Shuai-Qing Jiang https://orcid.org/0009-0001-8155-7905
Dong Xu https://orcid.org/0000-0003-3257-9435
Agnes P. C. van Hoof https://orcid.org/0009-0005-5404-2745
Wei-Hua Lei https://orcid.org/0000-0003-3440-1526
Hao Zhou https://orcid.org/0000-0003-2915-7434
Yong Chen https://orcid.org/0000-0001-9834-2196
Shao-Yu Fu https://orcid.org/0009-0002-7730-3985
Jun Yang https://orcid.org/0000-0002-5485-5042
Zi-Pei Zhu https://orcid.org/0000-0002-9022-1928
Alexei V. Filippenko https://orcid.org/0000-0003-3460-0103
Peter G. Jonker https://orcid.org/0000-0001-5679-0695
A. S. Pozanenko https://orcid.org/0000-0001-9435-1327
He Gao https://orcid.org/0000-0002-3100-6558
Xue-Feng Wu https://orcid.org/0000-0002-6299-1263
Bing Zhang https://orcid.org/0000-0002-9725-2524
Gavin P Lamb https://orcid.org/0000-0001-5169-4143
Massimiliano De Pasquale https://orcid.org/0000-0002-4036-7419
Shiho Kobayashi https://orcid.org/0000-0001-7946-4200
Franz Erik Bauer https://orcid.org/0000-0002-8686-8737
Hui Sun https://orcid.org/0000-0002-9615-1481
Giovanna Pugliese https://orcid.org/0000-0003-3457-9375
Valerio D'Elia https://orcid.org/0000-0003-3703-4418
Johan P. U. Fynbo https://orcid.org/0000-0002-8149-8298
WeiKang Zheng https://orcid.org/0000-0002-2636-6508
Alberto J. Castro-Tirado https://orcid.org/0000-0003-2999-3563
Yi-Han Iris Yin https://orcid.org/0000-0002-5596-5059

Yuan-Chuan Zou https://orcid.org/0000-0002-5400-3261
Adam T. Deller https://orcid.org/0000-0001-9434-3837
A. S. Moskvitin https://orcid.org/0000-0003-3244-6616
Sh. A. Egamberdiyev https://orcid.org/0000-0001-9730-3769
Andrew J. Levan https://orcid.org/0000-0001-7821-9369
Daniele Bjørn Malesani https://orcid.org/0000-0002-7517-326X
Maria E. Ravasio https://orcid.org/0000-0003-3193-4714
Jonathan Quirola-Vásquez https://orcid.org/0000-0001-8602-4641
Joyce N. D. van Dalen https://orcid.org/0009-0007-6927-7496
Javi Sánchez-Sierras https://orcid.org/0000-0003-2276-4231
Daniel Mata Sánchez https://orcid.org/0000-0003-0245-9424
Stuart P. Littlefair https://orcid.org/0000-0001-7221-855X
Jennifer A. Chacón https://orcid.org/0009-0000-6374-3221
Manuel A. P. Torres https://orcid.org/0000-0002-5297-2683
Ashley A. Chrimes https://orcid.org/0000-0001-9842-6808
Nikhil Sarin https://orcid.org/0000-0003-2700-1030
Antonio Martin-Carrillo https://orcid.org/0000-0001-5108-0627
Vik Dhillon https://orcid.org/0000-0003-4236-9642
Yi Yang https://orcid.org/0000-0002-6535-8500
Thomas G. Brink https://orcid.org/0000-0001-5955-2502
Rebecca L. Davies https://orcid.org/0000-0002-3324-4824
Sheng Yang https://orcid.org/0000-0002-2898-6532
Amar Aryan https://orcid.org/0000-0002-9928-0369
Ting-Wan Chen https://orcid.org/0000-0002-1066-6098
Albert K. H. Kong https://orcid.org/0000-0002-5105-344X
Wen-Xiong Li https://orcid.org/0000-0002-0096-3523
Rui-Zhi Li https://orcid.org/0000-0002-4205-0933
Jirong Mao https://orcid.org/0000-0002-7077-7195
Joseph Farah https://orcid.org/0000-0003-4914-5625
Zhou Fan https://orcid.org/0000-0003-3067-3540
D. Andrew Howell https://orcid.org/0000-0003-4253-656X
Dieter Hartmann https://orcid.org/0000-0002-8028-0991
Jing-Wei Hu https://orcid.org/0000-0002-0779-1947
Páll Jakobsson https://orcid.org/0000-0002-9404-5650
Cheng-Kui Li https://orcid.org/0000-0001-5798-4491
Curtis McCully https://orcid.org/0000-0001-5807-7893
Megan Newsome https://orcid.org/0000-0001-9570-0584
Benjamin Schneider https://orcid.org/0000-0003-4876-7756
Kaew Samaporn Tinyanont https://orcid.org/0000-0002-1481-4676
Ning-Chen Sun https://orcid.org/0000-0002-4731-9698
Giacomo Terreran https://orcid.org/0000-0003-0794-5982
Qing-Wen Tang https://orcid.org/0000-0001-7471-8451
Bin-Bin Zhang https://orcid.org/0000-0003-4111-5958
Juan Zhang https://orcid.org/0000-0001-8869-0672

References

Abbott, B. P., Abbott, R., Abbott, T. D., et al. 2017, ApJL, 848, L12
Ahumada, T., Singer, L. P., Anand, S., et al. 2021, NatAs, 5, 917
Almeida, A., Anderson, S. F., Argudo-Fernández, M., et al. 2023, ApJS, 267, 44
An, Z.-H., Antier, S., Bi, X.-Z., et al. 2023, arXiv:2303.01203
Arnaud, K. A. 1996, in ASP Conf. Ser. 101, Astronomical Data Analysis Software and Systems V, ed. G. H. Jacoby & J. Barnes (San Francisco, CA: ASP), 17
Aryan, A., Kong, A. K. H., Hsiao, H. Y., et al. 2024, GCN, 37002, 1
Atteia, J. L., Heussaff, V., Dezalay, J. P., et al. 2017, ApJ, 837, 119
Balasubramanian, A., Eappachen, D., Quirola-Vasquez, J., Sahu, D. K., & Anupama, G. C. 2024, GCN, 37468, 1
Band, D. L. 1997, ApJ, 486, 928
Barkov, M. V., & Pozanenko, A. S. 2011, MNRAS, 417, 2161
Barraud, C., Olive, J. F., Lestrade, J. P., et al. 2003, A&A, 400, 1021
Beniamini, P., Piran, T., & Matsumoto, T. 2023, MNRAS, 524, 1386
Bennett, C. L., Larson, D., Weiland, J. L., & Hinshaw, G. 2014, ApJ, 794, 135
Bi, X., Mao, J., Liu, C., & Bai, J.-M. 2018, ApJ, 866, 97
Campana, S., Mangano, V., Blustin, A. J., et al. 2006, Natur, 442, 1008
Cash, W. 1979, ApJ, 228, 939
Cepa, J., Aguiar, M., Escalera, V. G., et al. 2000, Proc. SPIE, 4008, 623
Chen, Y., Cui, W., Han, D., et al. 2020, Proc. SPIE, 11444, 114445B
Cheng, H., Zhang, C., Ling, Z., et al. 2025, arXiv:2505.18939
Chevalier, R. A., & Li, Z.-Y. 2000, ApJ, 536, 195
Chevalier, R. A., Li, Z.-Y., & Fransson, C. 2004, ApJ, 606, 369
Conroy, C., & Gunn, J. E. 2010, ApJ, 712, 833
Conroy, C., Gunn, J. E., & White, M. 2009, ApJ, 699, 486
Della Valle, M., Chincarini, G., Panagia, N., et al. 2006, Natur, 444, 1050
Dey, A., Schlegel, D. J., Lang, D., et al. 2019, AJ, 157, 168
Filippenko, A. V. 1982, PASP, 94, 715
Foreman-Mackey, D., Hogg, D. W., Lang, D., & Goodman, J. 2013, PASP, 125, 306
Fu, S. Y., An, J., Tinyanont, S., et al. 2024a, GCN, 36998, 1
Fu, S.-Y., Xu, D., Lei, W.-H., et al. 2024b, ApJ, 977, 197
Fynbo, J. P. U., Watson, D., Thöne, C. C., et al. 2006, Natur, 444, 1047
Galama, T. J., Vreeswijk, P. M., van Paradijs, J., et al. 1998, Natur, 395, 670
Galama, T. J., Vreeswijk, P. M., van Paradijs, J., et al. 1999, A&AS, 138, 465
Gao, H., Lei, W.-H., Zou, Y.-C., Wu, X.-F., & Zhang, B. 2013, NewAR, 57, 141
Gehrels, N., Norris, J. P., Barthelmy, S. D., et al. 2006, Natur, 444, 1044
Geng, J. J., Wu, X. F., Huang, Y. F., & Yu, Y. B. 2013, ApJ, 779, 28
Granot, J., Guetta, D., & Gill, R. 2017, ApJL, 850, L24
Granot, J., Panaitescu, A., Kumar, P., & Woosley, S. E. 2002, ApJL, 570, L61
Granot, J., & Sari, R. 2002, ApJ, 568, 820
Huang, Y. F., Gou, L. J., Dai, Z. G., & Lu, T. 2000, ApJ, 543, 90
Ioka, K., & Nakamura, T. 2018, PTEP, 2018, 043E02
Johnson, B. D., Leja, J., Conroy, C., & Speagle, J. S. 2021, ApJS, 254, 22
Kobayashi, S. 2000, ApJ, 545, 807
Kobayashi, S., Piran, T., & Sari, R. 1999, ApJ, 513, 669
Kobayashi, S., & Zhang, B. 2003, ApJ, 597, 455
Kouveliotou, C., Meegan, C. A., Fishman, G. J., et al. 1993, ApJL, 413, L101
Kumar, P., & Zhang, B. 2015, PhR, 561, 1
Lamb, G. P., & Kobayashi, S. 2019, MNRAS, 489, 1820
Lamb, G. P., Tanvir, N. R., Levan, A. J., et al. 2019, ApJ, 883, 48
Lang, D., Hogg, D. W., Mierle, K., Blanton, M., & Roweis, S. 2010, AJ, 139, 1782
Lei, W.-H., Yuan, Q., Zhang, B., & Wang, D. 2016, ApJ, 816, 20
Lei, W.-H., Zhang, B., & Liang, E.-W. 2013, ApJ, 765, 125
Lei, W.-H., Zhang, B., Wu, X.-F., & Liang, E.-W. 2017, ApJ, 849, 47
Levan, A. J., Gompertz, B. P., Salafia, O. S., et al. 2024, Natur, 626, 737
Liddle, A. R. 2007, MNRAS, 377, L74
Liu, T., Hou, S.-J., Xue, L., & Gu, W.-M. 2015, ApJS, 218, 12
Meegan, C., Lichti, G., Bhat, P. N., et al. 2009, ApJ, 702, 791
Mészáros, P., & Rees, M. J. 1997, ApJ, 476, 232
Nava, L., Sironi, L., Ghisellini, G., Celotti, A., & Ghirlanda, G. 2013, MNRAS, 433, 2107
Norris, J. P., Marani, G. F., & Bonnell, J. T. 2000, ApJ, 534, 248
O'Connor, B., Troja, E., Ryan, G., et al. 2023, SciA, 9, eadi1405
Oke, J. B., Cohen, J. G., Carr, M., et al. 1995, PASP, 107, 375
Oke, J. B., & Gunn, J. E. 1983, ApJ, 266, 713
Paciesas, W. S., Meegan, C. A., Pendleton, G. N., et al. 1999, ApJS, 122, 465
Pérez-Fournon, I., Poidevin, F., Aguado, D. S., et al. 2024, GCN, 37007, 1
Perley, D. A. 2019, PASP, 131, 084503
Peterson, B. M., Wanders, I., Horne, K., et al. 1998, PASP, 110, 660
Quirola-Vásquez, J., van Dalen, J., Malesani, D. B., et al. 2024, GCN, 37013, 1
Rastinejad, J. C., Gompertz, B. P., Levan, A. J., et al. 2022, Natur, 612, 223
Rees, M. J., & Meszaros, P. 1992, MNRAS, 258, 41
Rhodes, L., van der Horst, A. J., Bright, J. S., et al. 2024, MNRAS, 533, 4435
Sakamoto, T., Hullinger, D., Sato, G., et al. 2008, ApJ, 679, 570
Sari, R., & Piran, T. 1999, ApJ, 520, 641
Sari, R., Piran, T., & Narayan, R. 1998, ApJL, 497, L17
Sato, Y., Obayashi, K., Yamazaki, R., Murase, K., & Ohira, Y. 2021, MNRAS, 504, 5647
Sazonov, S. Y., Lutovinov, A. A., & Sunyaev, R. A. 2004, Natur, 430, 646
Scargle, J. D., Norris, J. P., Jackson, B., & Chiang, J. 2013, ApJ, 764, 167
Schlafly, E. F., & Finkbeiner, D. P. 2011, ApJ, 737, 103
Schwarz, G. 1978, AnSta, 6, 461
Science Software Branch at STScI 2012, PyRAF: Python Alternative for IRAF, Astrophysics Source Code Library, ascl:1207.011
Skrutskie, M. F., Cutri, R. M., Stiening, R., et al. 2006, AJ, 131, 1163
Tody, D. 1986, Proc. SPIE, 627, 733
Troja, E., Fryer, C. L., O'Connor, B., et al. 2022, Natur, 612, 228
Ukwatta, T. N., Stamatikos, M., Dhuga, K. S., et al. 2010, ApJ, 711, 1073
Urata, Y., Huang, K., Yamazaki, R., & Sakamoto, T. 2015, ApJ, 806, 222

van Dokkum, P. G. 2001, PASP, 113, 1420
Van Eerten, H. J., & Wijers, R. A. M. J. 2009, MNRAS, 394, 2164
Vianello, G., Lauer, R. J., Younk, P., et al. 2015, arXiv:1507.08343
Willingale, R., Starling, R. L. C., Beardmore, A. P., Tanvir, N. R., & O'Brien, P. T. 2013, MNRAS, 431, 394
Wilms, J., Allen, A., & McCray, R. 2000, ApJ, 542, 914
Woosley, S. E., & Bloom, J. S. 2006, ARA&A, 44, 507
Wu, X. F., Dai, Z. G., Huang, Y. F., & Lu, T. 2003, MNRAS, 342, 1131
Yamazaki, R., Ioka, K., & Nakamura, T. 2002, ApJ, 571, L31
Yamazaki, R., Yonetoku, D., & Nakamura, T. 2003, ApJ, 594, L79
Yang, B., Jin, Z.-P., Li, X., et al. 2015, NatCo, 6, 7323
Yang, Y.-H., Troja, E., O'Connor, B., et al. 2024, Natur, 626, 742
Yuan, W., Dai, L., Feng, H., et al. 2025, SCPMA, 68, 239501
Yuan, W., Zhang, C., Chen, Y., & Ling, Z. 2022, in The Einstein Probe Mission, ed. C. Bambi & A. Santangelo (Singapore: Springer Nature), 1
Zhang, B. 2018, The Physics of Gamma-Ray Bursts (Cambridge: Cambridge Univ. Press)
Zhang, B., & Kobayashi, S. 2005, ApJ, 628, 315
Zhang, B., Kobayashi, S., & Mészáros, P. 2003, ApJ, 595, 950
Zhang, B., & Mészáros, P. 2001, ApJL, 552, L35
Zhang, B., & Mészáros, P. 2004, IJMPA, 19, 2385
Zhang, B., Wang, X.-Y., & Zheng, J.-H. 2024, JHEAp, 41, 42
Zhang, B., Zhang, B.-B., Virgili, F. J., et al. 2009, ApJ, 703, 1696
Zhang, B. B., Liu, Z. K., Peng, Z. K., et al. 2021, NatAs, 5, 911
Zheng, W., Brink, T. G., Filippenko, A. V., et al. 2024, GCN, 37228, 1
Zhou, C., Zhu, Z.-P., Lei, W.-H., et al. 2024, ApJ, 963, 66
Zhou, H., Wang, W. X., Hu, J. W., et al. 2024, GCN, 36997, 1
Zhou, R., Newman, J. A., Mao, Y.-Y., et al. 2021, MNRAS, 501, 3309
Zhu, Z.-P., Xu, D., Fynbo, J. P. U., et al. 2023, ApJ, 948, 30
Zou, Y. C., Wu, X. F., & Dai, Z. G. 2005, MNRAS, 363, 93